

Extraction of Single and Double Differential Cross-Sections on Argon for CC1 μ 2p0 π Event Topologies in the SBND

Emilio Peláez Cisneros

July 19, 2024

Abstract

The precise measurement of cross-sections for a variety of interactions is critical to the success of upcoming flagship neutrino experiments. Of special interest are neutrino interactions that leave the nucleus in a 2-particle 2-hole state (2p2h). This note will present cross-section measurements for the production of 2p2h states on Argon. Using SBND data collected from the **period** of operation, we select events corresponding to a charged-current ν_μ interaction that left the Argon nucleus in a 2p2h state. These interactions produce a topology with one muon and two protons in the final state (CC1 μ 2p0 π). This analysis targets both single differential and double differential cross-section measurements for CC1 μ 2p0 π event topologies in a variety of kinematic variables. Comparisons are made to a set of theoretical models that explore different cross-section modeling configurations. Code for this analysis is available on [GitHub](#).

Contents

1 Generator analysis	2
1.1 Signal definition	2
1.2 Generators	2
1.3 Variables definition	3
1.4 Pre-FSI events	3
1.5 Double differential plots	3
1.6 Pure MEC events	13
2 SBND analysis	15
2.1 Fiducial volume	15
2.2 Signal definition	15
2.3 Variable plots	16
2.4 Signal efficiency	16
2.5 Migration and response matrices	16
2.6 Systematics	16
3 Closure test	29
4 Cross-section results	29
5 Appendices	32
5.1 Cross section systematics	32
6 References	45

1 Generator analysis

2 1.1 Signal definition

3 We choose charged-current muon neutrino interactions that result in one muon, two protons, no charged pions
4 with $P_\pi > 70$ MeV/c, no neutral pions or heavier mesons, and any number of neutrons. These interactions
5 are denoted as $\text{CC}1\mu2\text{p}0\pi$. We require the momentum of the muon and protons to be in the following ranges
6 (in MeV/c):

$$100 < P_P < 1200 \quad 300 < P_\mu < 1000 \quad (1)$$

7 1.2 Generators

8 The following generators are used to create events, which are then discriminated using the signal defini-
9 tion above: NuWro, GiBUU, NEUT, GENIE G18, GENIE AR23. Information about these generators is
10 summarized in Table 1.

Name	Generator/Configuration
G18	GENIE v3.0.6 G18_10a_02_11a
AR23	G18 with SuSAv2 MEC model
NuWro	NuWro 19.02.1
NEUT	NEUT v5.4.0
GiBUU	GiBUU 2021

Table 1: Generator and configuration data.

11 The GENIE configurations we used are:

- 12 (i) GENIE G18 [1, 2]: This modern model configuration uses the local Fermi gas (LFG) model [8],
13 the Nieves CCQE scattering prescription [18], which includes Coulomb corrections for the outgoing
14 muon [9], and random phase approximation (RPA) corrections [17]. Additionally, it uses the
15 Nieves MEC model [20], the KuzminLyubushkin-Naumov Berger-Sehgal RES [5, 22, 13], Berger-Sehgal
16 COH [6] and Bodek-Yang DIS [23] scattering models with the PYTHIA [21] hadronization part, and
17 the hA2018 FSI model [3].
- 18 (ii) GENIE AR23: Same as the G18 model configuration but using the SuSAv2 MEC model.

19 The alternative event generators are:

- 20 (i) NuWro [10]: Includes the LFG model [8], the Llewellyn Smith model for QE events [15], the Nieves
21 model for MEC events [19], the AdlerRarita-Schwinger formalism to calculate the Δ resonance explicitly
22 [11], the Berger-Sehgal (BS) COH [6] scattering model, an intranuclear cascade model for FSI [19],
23 and a coupling to PYTHIA [21] for hadronization.
- 24 (ii) NEUT [12]: Corresponds to the combination of the LFG model [7, 8], the Nieves CCQE scattering
25 prescription [18], the Nieves MEC model using a lookup table [20], the Berger Sehgal RES [5, 11, 4]
26 and BS COH [6] scattering models, FSI with medium corrections for pions [1, 2], and PYTHIA [21]
27 purposes.
- 28 (iii) GiBUU [16]: Uses similar models to GENIE, but they are implemented in a coherent way by solving
29 the Boltzmann-Uehling-Uhlenbeck transport equation [16]. The modeling includes the LFG model [8],
30 a standard CCQE expression [14], an empirical MEC model, and a dedicated spin dependent resonance
31 amplitude calculation following the MAID analysis [16]. The DIS model is from PYTHIA [21]. GiBUU's
32 FSI treatment propagates the hadrons through the residual nucleus in a nuclear potential consistent
33 with the initial state.

34 1.3 Variables definition

35 Given the momentum vectors for the leading proton \vec{p}_L , recoil proton \vec{p}_R , and muon \vec{p}_μ , we define several
 36 variables. First, we define the momenta and opening angle of each variable, denoted as $|\vec{p}|$ and $\cos(\theta_{\vec{p}})$, with
 37 the appropriate index for each momentum vector. These variables are plotted in Figure 1.

38 We also define variables relating the multiple momentum vectors. First, the opening angle between the
 39 protons in the lab frame, given by

$$\cos(\theta_{\vec{p}_L, \vec{p}_R}) = \frac{\vec{p}_L \cdot \vec{p}_R}{|\vec{p}_L||\vec{p}_R|}. \quad (2)$$

40 Then, the opening angle between the total proton momentum ($\vec{p}_{\text{sum}} = \vec{p}_L + \vec{p}_R$) and the muon, given by

$$\cos(\theta_{\vec{p}_\mu, \vec{p}_{\text{sum}}}) = \frac{\vec{p}_\mu \cdot \vec{p}_{\text{sum}}}{|\vec{p}_\mu||\vec{p}_{\text{sum}}|}. \quad (3)$$

41 The momentum transverse to the direction of the neutrino beam, which we denote $\delta\vec{P}_T$ and is given by

$$\delta\vec{P}_T = \vec{p}_T^\mu + \vec{p}_T^L + \vec{p}_T^R. \quad (4)$$

42 For the transverse momentum, we will be interested in its magnitude $|\delta\vec{P}_T|$. Finally, the angular orientation
 43 of the transverse momentum with respect to the transverse muon is defined as

$$\delta\alpha_T = \cos^{-1} \left(\frac{-\vec{p}_T^\mu \cdot \delta\vec{P}_T}{|\vec{p}_T^\mu||\delta\vec{P}_T|} \right). \quad (5)$$

44 We plot the differential cross sections of these variables for the given generators in Figure 2. We can also
 45 see the cross section by event type for $|\delta\vec{P}_T|$ for the all generators in Figure 3. We only show one variable
 46 for the interaction breakdown, as the percentages will remain the same for other variables.

47 1.4 Pre-FSI events

48 To investigate why the percentage of MEC events for some generators is low, we performed event selection
 49 before any final state interactions took place. For both GENIE tunes, NEUT, and NuWro, we got 100%
 50 MEC events pre-FSI. For GiBUU, only 4.1% MEC versus 76.2% RES and 16% DIS events pre-FSI. The
 51 interaction breakdown plots for all the generators are shown in Figure 4. Again, only one variable is shown
 52 as the percentages will remain the same for others. Since GiBUU is the outlier, we checked the specific
 53 interaction mode for the resonance events. We got that 10 has 39.3%, 11 has 34.7%, 12 has 0.0136%, 13 has
 54 26 %, and 27, 22, and 23 all have zero percent of the resonance events. We also checked the event interaction
 55 breakdown for GiBUU samples without final state interactions, in which we found that 100% of the events
 56 are MEC, shown in Figure 5.

57 1.5 Double differential plots

58 For our double differential figures, we plot δP_T , $\delta\alpha_T$, $\cos(\theta_{\vec{p}_L, \vec{p}_R})$, and $\cos(\theta_{\vec{p}_\mu, \vec{p}_{\text{sum}}})$ in $\cos(\theta_{\vec{p}_\mu})$. These are
 59 shown in Figure 6. We have two bins for $\cos(\theta_{\vec{p}_\mu})$, the first one going from -1 to 0.5 and the second from 0.5
 60 to 1. Therefore, these are irregular bins, with the first holding a larger range than the first. The interaction
 61 breakdown for $\delta\alpha_T$ in $\cos(\theta_{\vec{p}_\mu})$ is shown in Figure 7.

62 We also slice the double differential plots into two plots each, so that we have $\cos(\theta_{\vec{p}_\mu})$ in the horizontal
 63 axis instead of bin numbers. These plots are shown in Figure 8. In these plots, the bins contents have been
 64 reweighted appropriately, by dividing the content of each bin by the width of the bin for the variable in
 65 the axis multiplied by the width of the $\cos(\theta_{\vec{p}_\mu})$ slice. Note that the plots for the $0.5 < \cos(\theta_{\vec{p}_\mu}) < 1$ slice
 66 have more events in general, although they span a smaller phase space of $\cos(\theta_{\vec{p}_\mu})$, as it can be seen by the
 67 scale of the vertical axis. We performed the same double differential analysis for the events before final state
 68 interactions. These are shown in Figure 9.

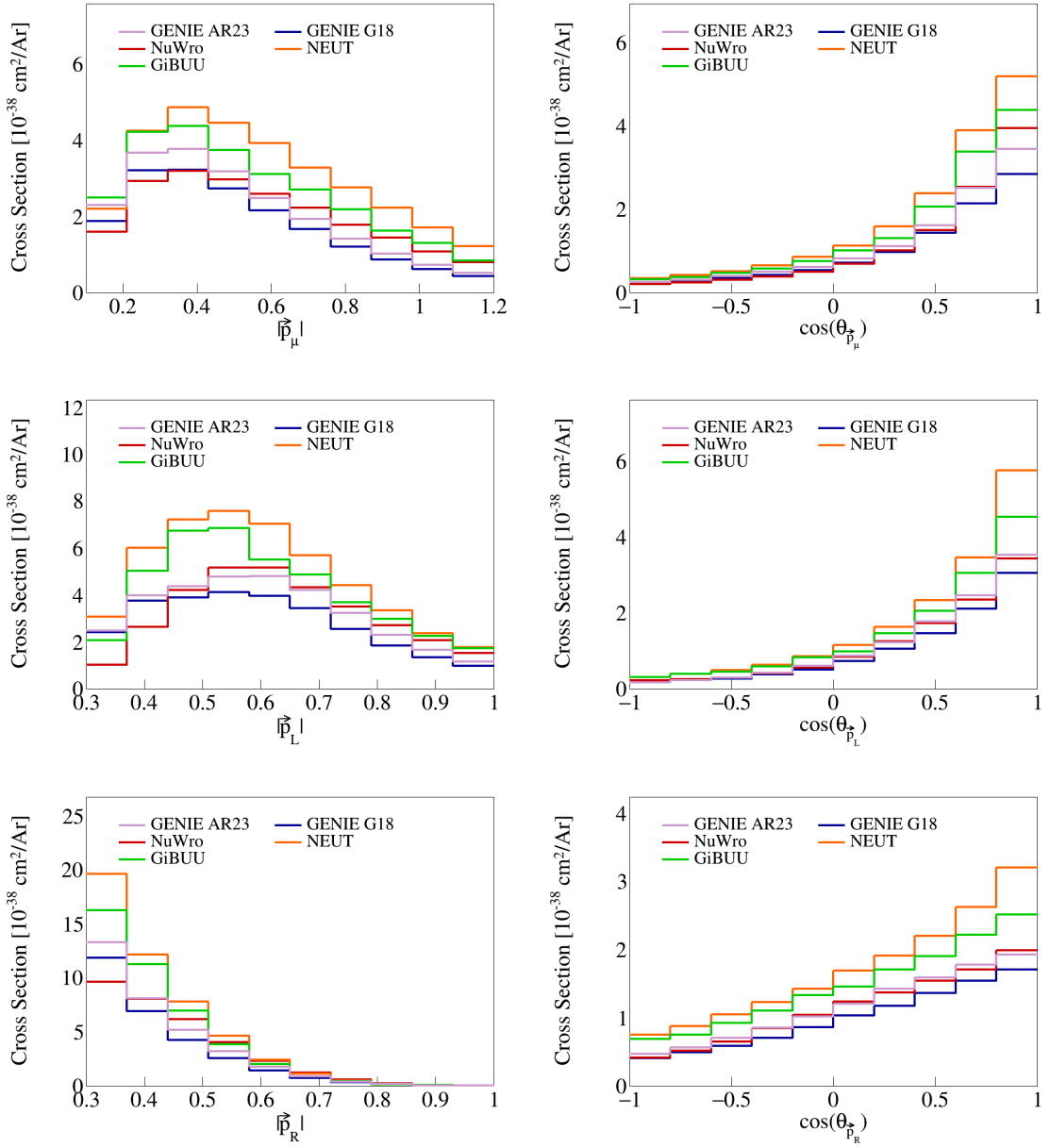


Figure 1: Cross sections for momentum and opening angles of individual particles.

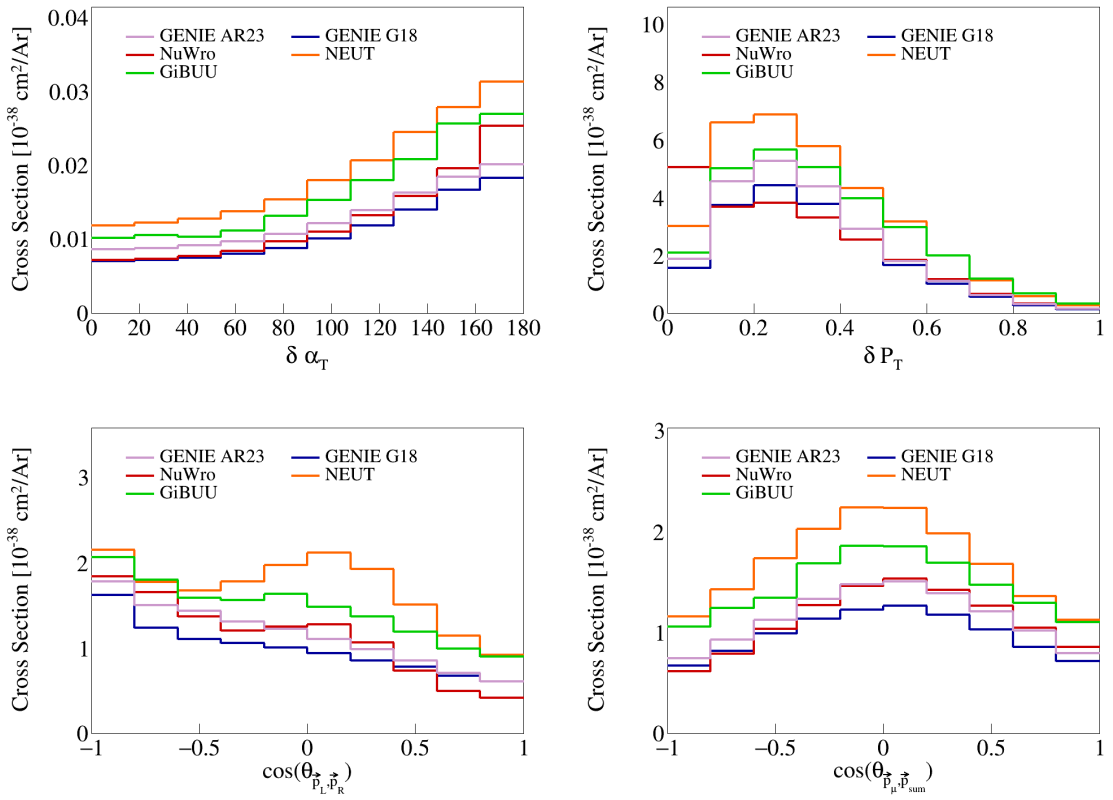


Figure 2: Cross sections for opening angles and transverse momentum.

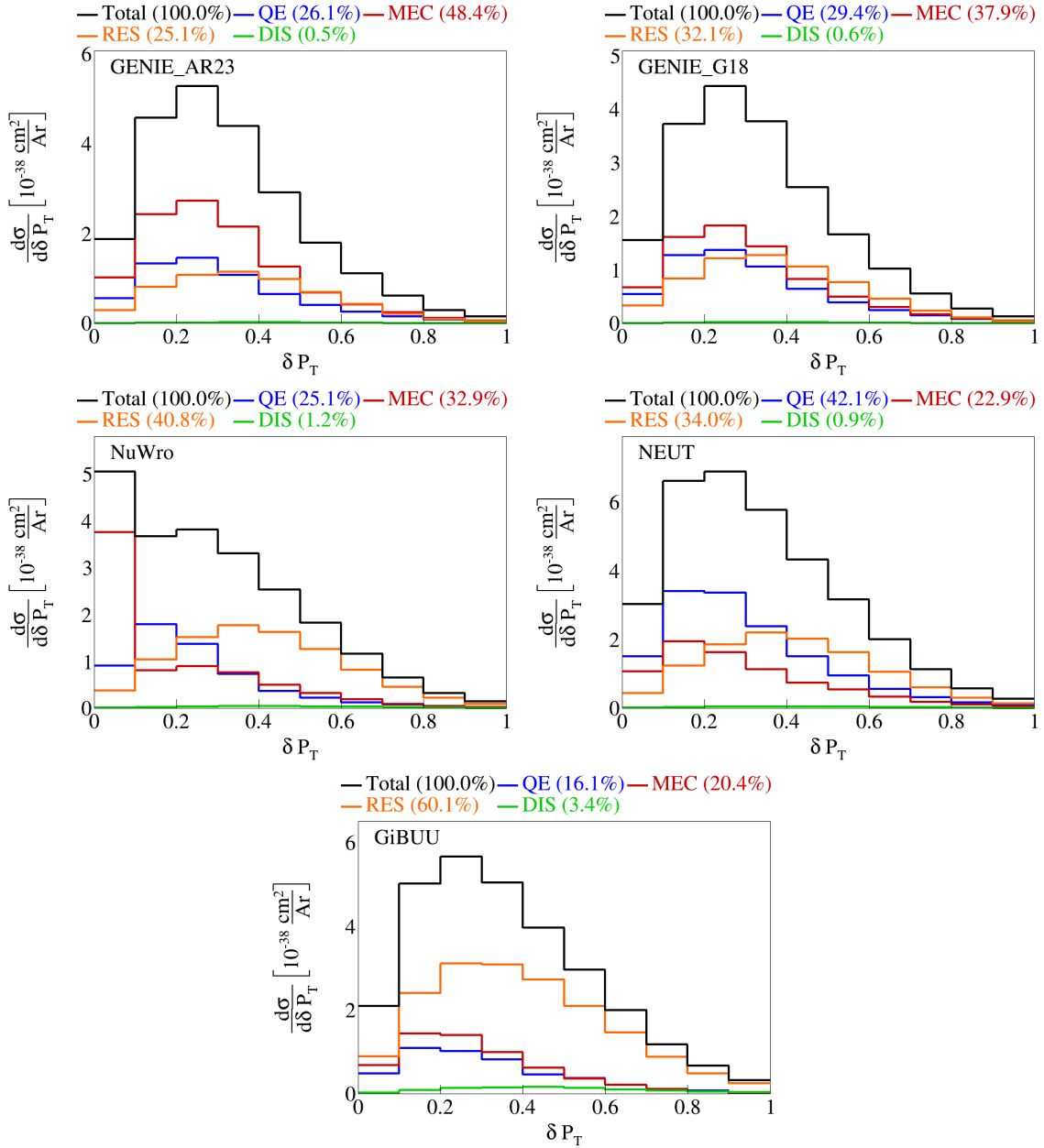


Figure 3: Event interaction breakdown for $|\delta \vec{P}_T|$.

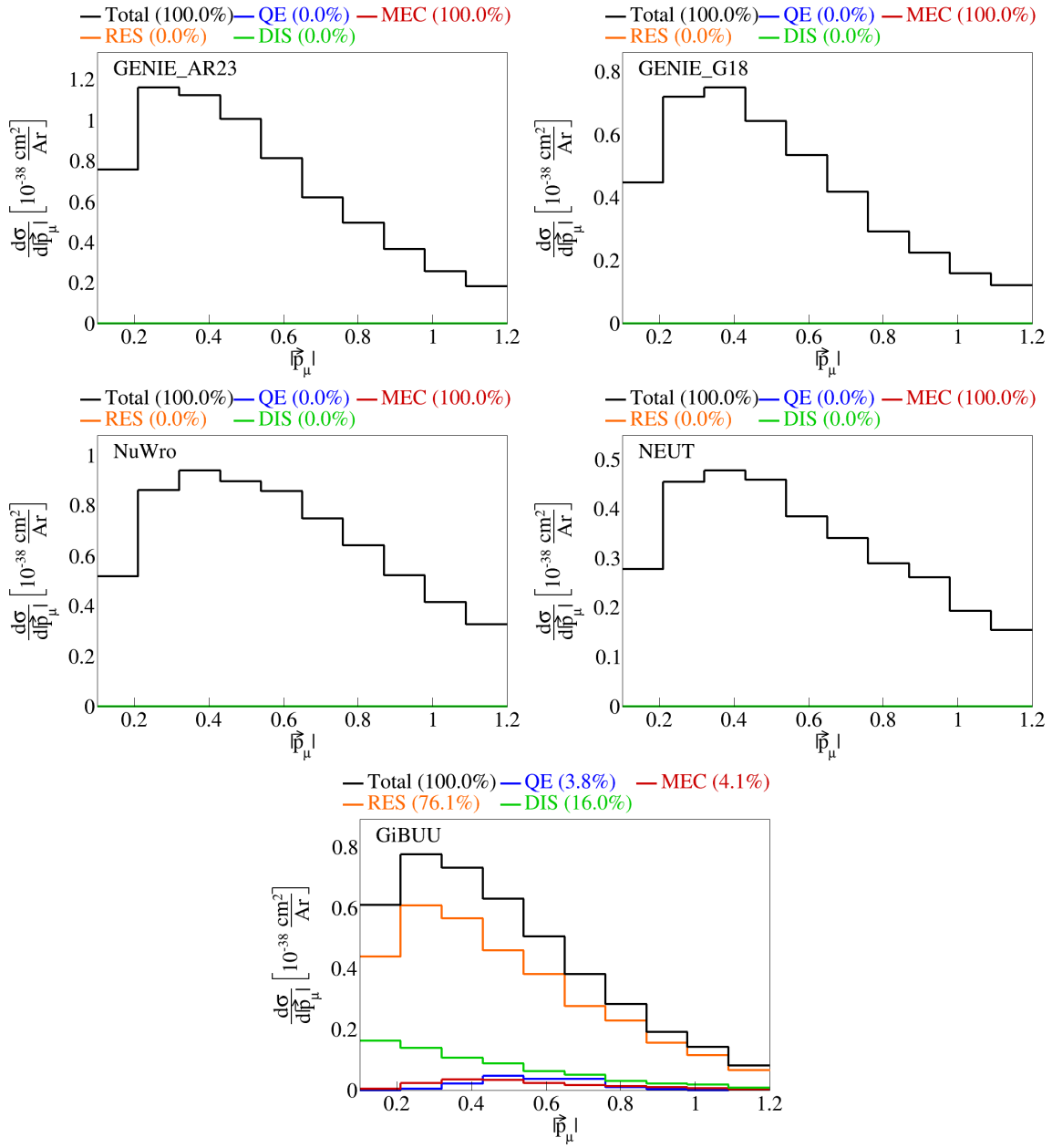


Figure 4: Event interaction breakdown of $|\vec{p}_\mu|$ before final state interactions.

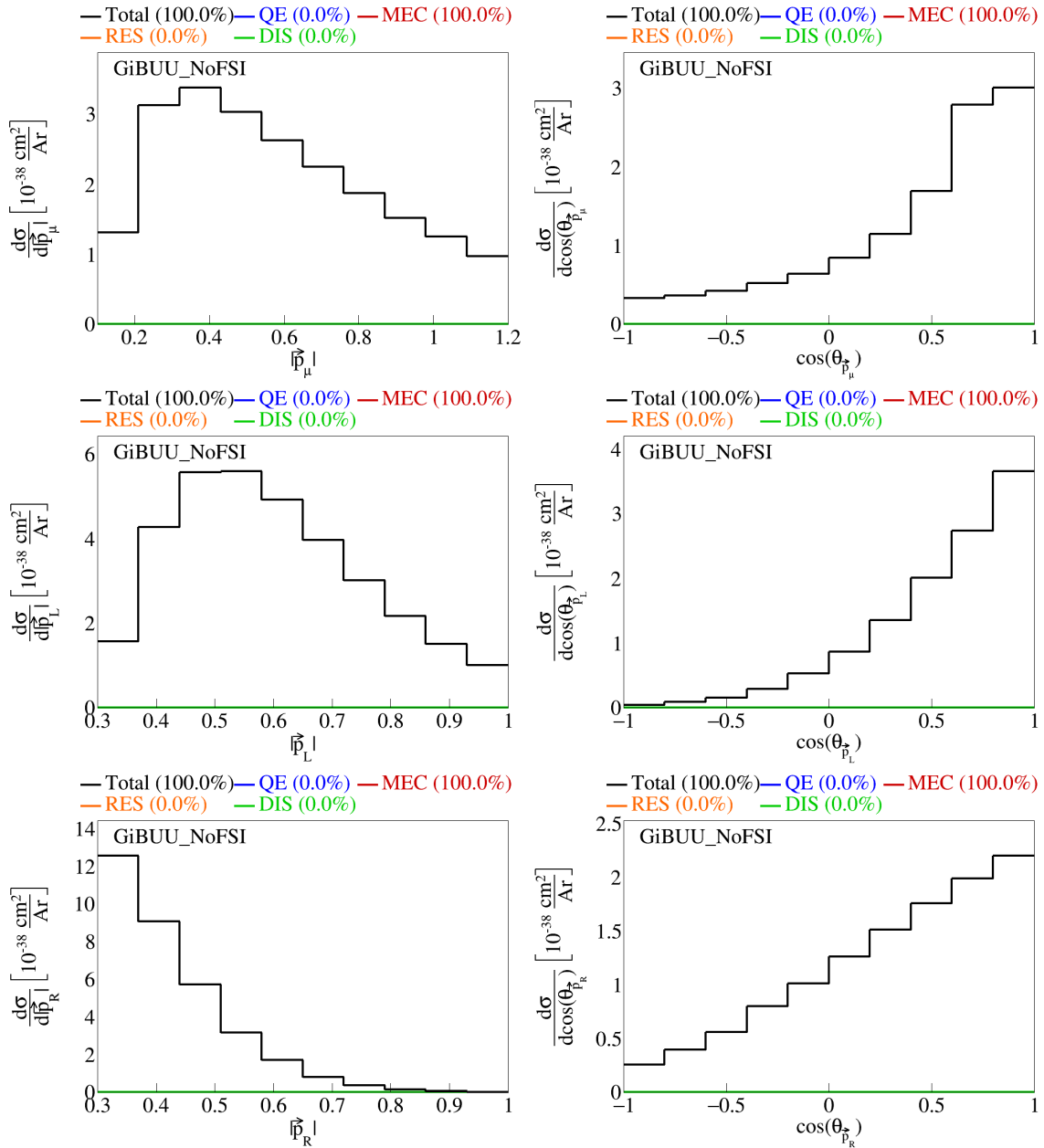


Figure 5: Event interaction breakdown for final events from GiBUU events with no FSI.

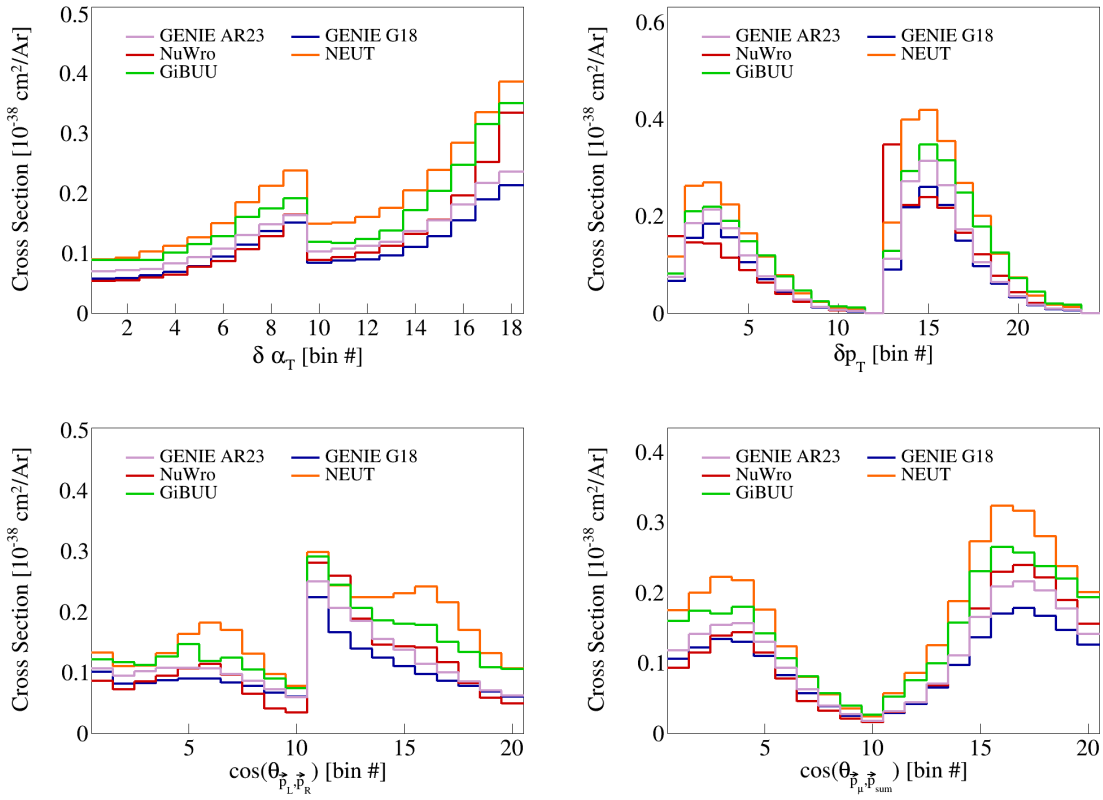


Figure 6: Double differential serial plots, all in $\cos(\theta_{\vec{p}_\mu})$.

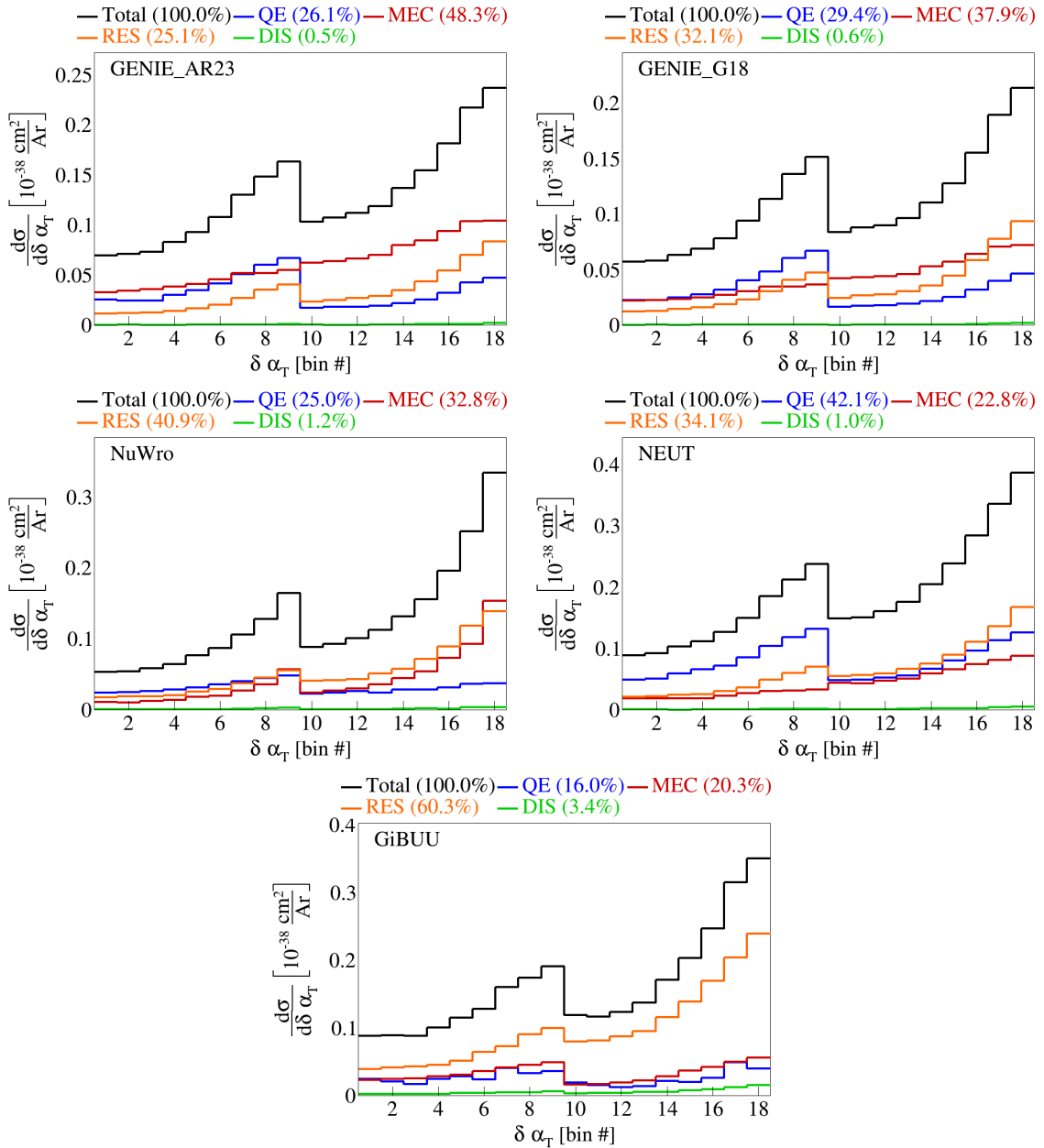


Figure 7: Interaction breakdown for $\delta\alpha_T$ in $\cos(\theta_{\vec{p}_\mu})$.

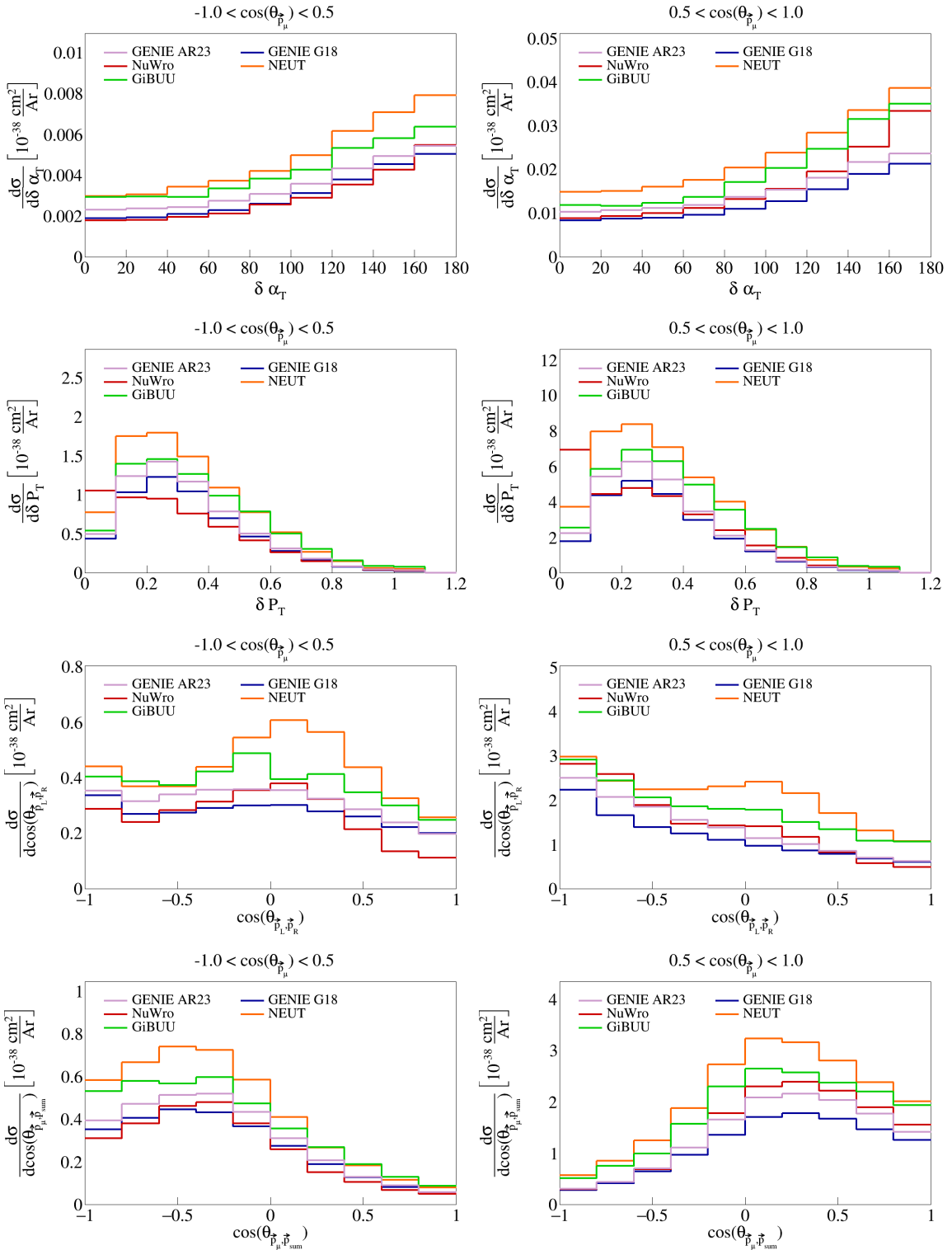


Figure 8: Sliced double differential plots.

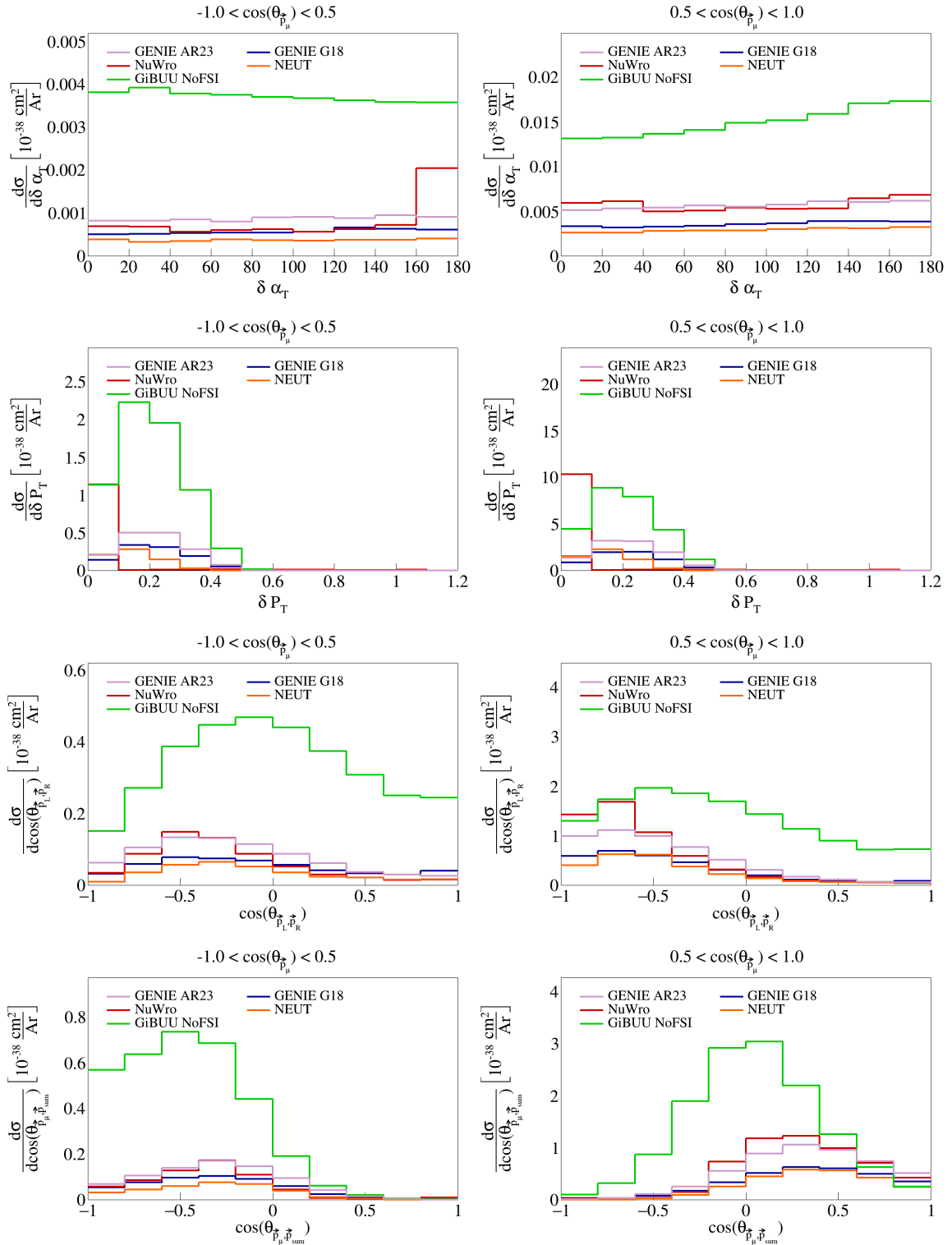


Figure 9: Sliced double differential plots for pre-FSI events.

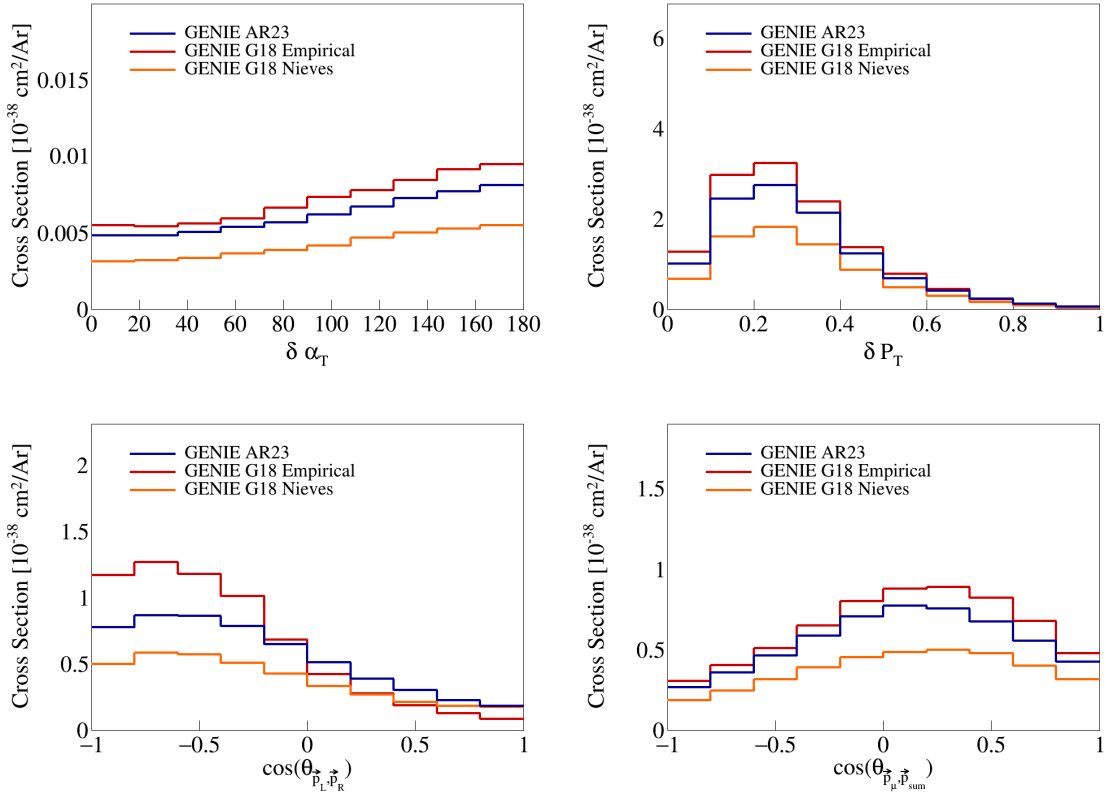


Figure 10: Transverse kinematic variables for pure MEC events.

69 1.6 Pure MEC events

70 We also generated pure MEC events with different configurations to get the MEC splines. These were all
 71 different tunes of GENIE: AR23, G18 with Empirical MEC model, and G18 with Nieves MEC model. The
 72 plots for the transverse kinematic variables are shown in Figure 10. The sliced double differential plots are
 73 shown in Figure 11.

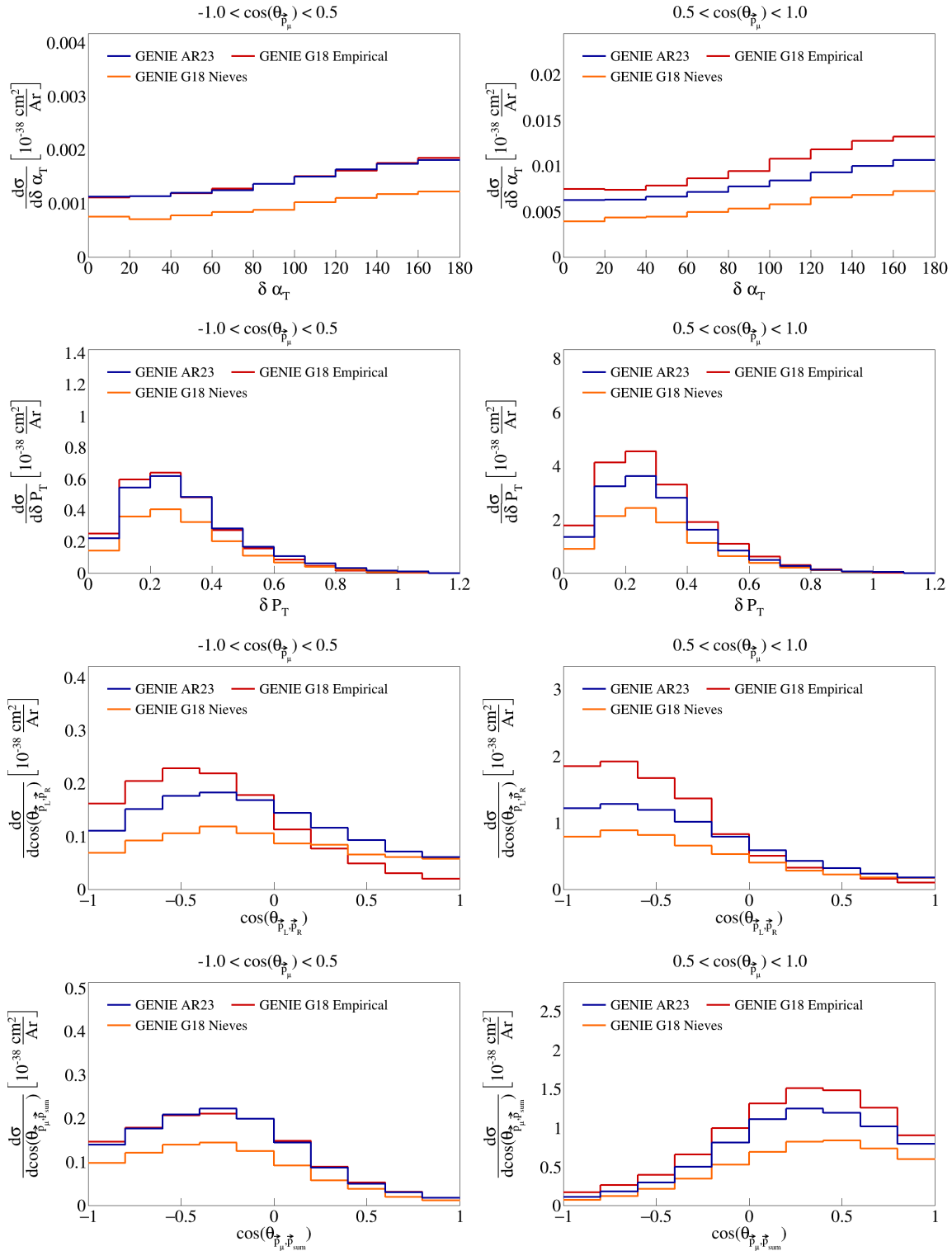


Figure 11: Sliced double differential plots for pure MEC events.

74 2 SBND analysis

75 The CAF files used for this analysis are available in the Fermilab gpvms at the path

76 /pnfs/sbnd/persistent/users/apapadop/CAF_Files/*.flat.caf.root

77 where the asterisk means that all the files in the directory with the extension .flat.caf.root will be used.

78 2.1 Fiducial volume

79 To perform the analysis of SBND data, we have to define the fiducial volume of the detector, which represents
80 a central part of the detector in which we will accept signals. The fiducial volume is given by the following
81 ranges:

$$5 < |x| < 180 \quad |y| < 180 \quad 10 < z < 450 \quad (6)$$

82 where x , y , and z are the coordinates in the detector frame, all in centimeters.

83 2.2 Signal definition

84 To perform analysis on experiment data, we will be using the CAFAna framework. This allows us to perform
85 cuts based on the reconstructed and Monte Carlo data (if available, i.e., only in the case of dealing with
86 simulated events), to discriminate events. To discriminate events based on their Monte Carlo data, we
87 perform a simple `TruthCut` that checks the following:

- 88 (i) That the neutrino interaction takes place in the fiducial volume
- 89 (ii) That the neutrino is a muon neutrino
- 90 (iii) That the interaction is a charged current interaction
- 91 (iv) That there is only one muon in our allowed momentum range
- 92 (v) That there are only two protons in our allowed momentum range
- 93 (vi) That there are no charged/neutral pions in our defined momenta ranges

94 Using the reconstructed event data, we can perform a `Cut` that checks the following:

- 95 (i) The reconstructed vertex for the neutrino interaction takes place in the fiducial volume
- 96 (ii) That the event is not a cosmic event by Pandora's criteria (using `nu_score` to check how neutrino like
97 the slice is, and `fmatch.score` with `fmatch.time` to check the event comes from the beam)
- 98 (iii) That there is one muon track with $L_{\text{track}} > 50$ cm, $\chi^2_\mu < 30$, $\chi^2_p > 60$, and this being the longest
99 reconstructed track, and that this has momentum in our allowed range
- 100 (iv) That there are two proton tracks with $\chi^2_p < 100$, and that these have momentum in our allowed range
- 101 (v) That there are no other reconstructed tracks with momentum in the allowed range for charged pions
- 102 (vi) That there are no reconstructed particles with a positive `trackScore` less than 0.5, so we don't allow
103 any neutral pions

104 Using these two discriminators on simulated events, the reconstructed events that satisfy the signal definition,
105 and distinguish between true signal events and background events. This is shown in more detail for all our
106 variables in the next section.

107 We use a one-bin histogram with lower bound 0 and upper bound of 3 in the true energy variable to get
108 total counts of generated events, true signal events, all reconstructed events, and efficiency and purity data
109 after each of the cuts we apply to the reconstructed events. These results are shown in Table 2. Counts
110 are obtained using ROOT's command `Histo->Integral()`. Global efficiency is defined as the ratio between
111 events that pass the cut and reconstructed events, signal efficiency as the ratio between true events that pass
112 the cut and the all true signal events, and purity as the ratio between true signal events that pass the cut
113 and all events that pass the cut. The numbers reported in this table are POT normalized to $6.6 \cdot 10^{20}$.

Cut	Number of events	Global efficiency	Signal efficiency	Purity
All	1.31823e7	-	-	-
True signal events	273751	-	-	-
All reco events	6.61683e6	100%	-	-
Cosmic cut	5.46987e6	82.6659%	89.0567%	4.45703%
Vertex in FV cut	3.10952e6	46.9941%	87.5899%	7.7111%
One muon cut	2.14513e06	32.4193%	69.629%	8.88571%
Two protons cut	137309	2.07514%	16.3503%	32.5975%
No charged pions cut	65938	0.99652%	12.1369%	50.3881%
No neutral pions cut	54088.9	0.817444%	10.929%	55.313%

Table 2: Global efficiency, selection efficiency, and purity for cuts made in signal definition.

114 2.3 Variable plots

115 Using all the variable definitions as we did when studying the event generators, and the signal definition
 116 based on the cuts described in the previous section, we can generate plots for SBND data. The reconstructed
 117 single differential variables corresponding to vector opening angles and magnitudes are shown in Figure 12.
 118 In these figures, three lines are shown, corresponding to: all reconstructed (all the reconstructed events that
 119 pass our signal definition), signal (reconstructed events that pass signal definition and are true signal events
 120 as determined by the `TruthCut` from our previous section), and background (reconstructed events that pass
 121 signal definition but are not true signal events) events. Similarly, the variables relating multiple vectors are
 122 shown in Figure 13, and double differential sliced variables are shown in Figure 14.

123 2.4 Signal efficiency

124 Using the truth information about reconstructed events, we can also compute signal efficiency on a bin-by-
 125 bin basis. To be precise, signal definition on a bin *i* is defined as the ratio between the number of events
 126 generated in bin *i* and reconstructed in any bin over the number of events generated in bin *i*. These plots
 127 are shown in Figure 15 and Figure 16 for single-differential variables and Figure 17 for double differential
 128 variables.

129 2.5 Migration and response matrices

130 Further, we compute migration matrices which give us a measure of how reliable our reconstructed variables
 131 are. A given column in this matrix represents a bin of the truth variable, i.e., the value with which the
 132 event was generated. Then, each row corresponds to a reconstructed bin of the same variable, and each cell
 133 corresponds to the probability that an event generated with the truth value corresponding to the column gets
 134 reconstructed with the value corresponding to the row. For the migration matrix, we consider true signal
 135 events that were reconstructed and satisfy our signal definition in the denominator. Therefore, the values in
 136 each column must add up to 1. The migration matrices for the single differential variables are presented in
 137 Figure 18 and Figure 19. The migration matrices for the double differential variables (given in terms of the
 138 bin number) are presented in Figure 20.

139 Response matrices are computed in a similar manner, but using the total number of generated events in the
 140 denominator when computing the ratios, i.e., without requiring the events to be successfully reconstructed.
 141 Therefore, for these matrices, the columns of the response matrices do not have to add up to 1. The response
 142 matrices for single differential variables are presented in Figure 21 and Figure 22, and the double differential
 143 response matrices are given in Figure 23.

144 2.6 Systematics

145 To include systematic uncertainties in our study, we first consider cross sectional systematics. These are
 146 variations in the cross section models used to generate the events. They can be of two types: multisigma

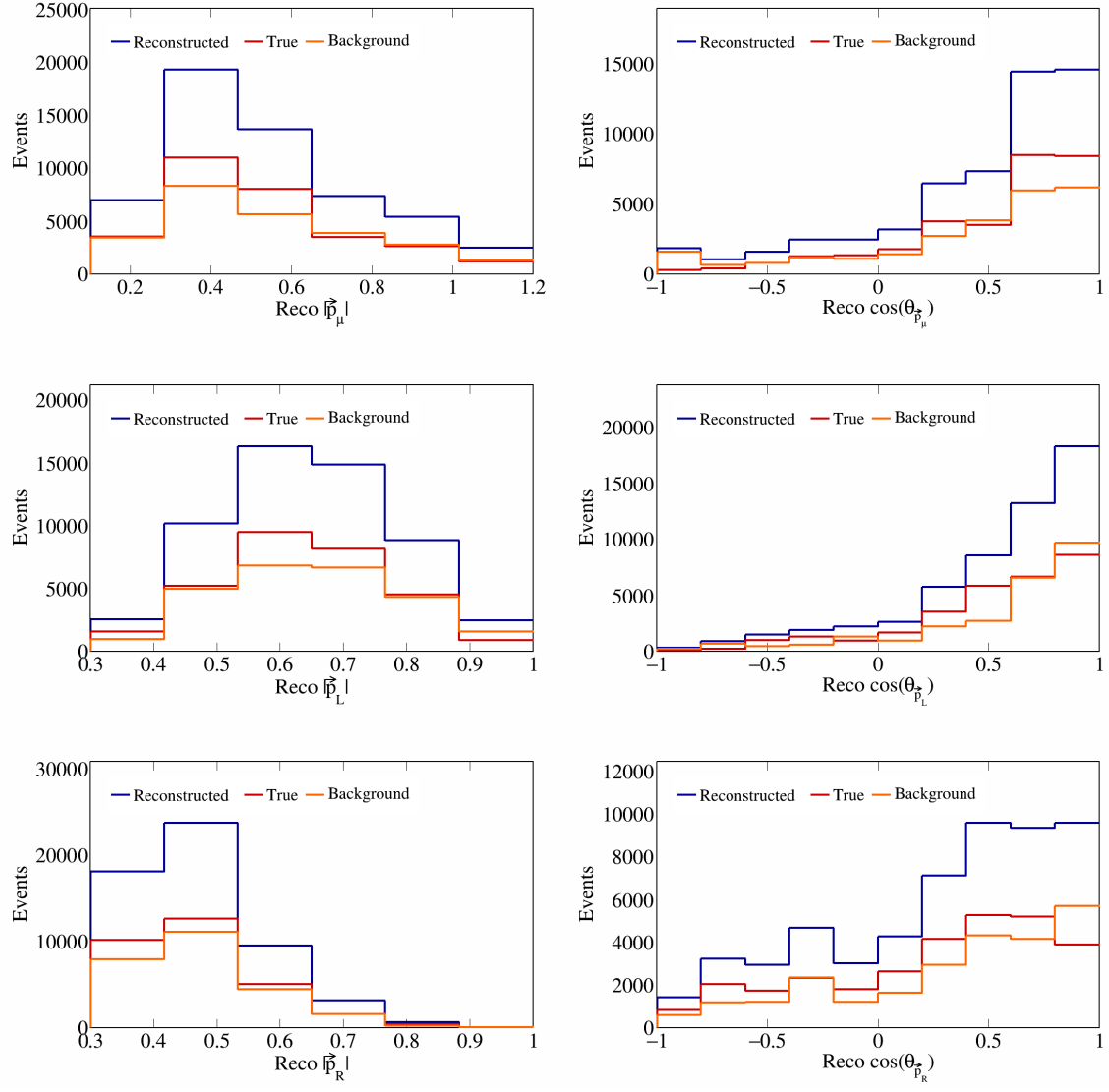


Figure 12: Vector directions and magnitudes for SBND data.

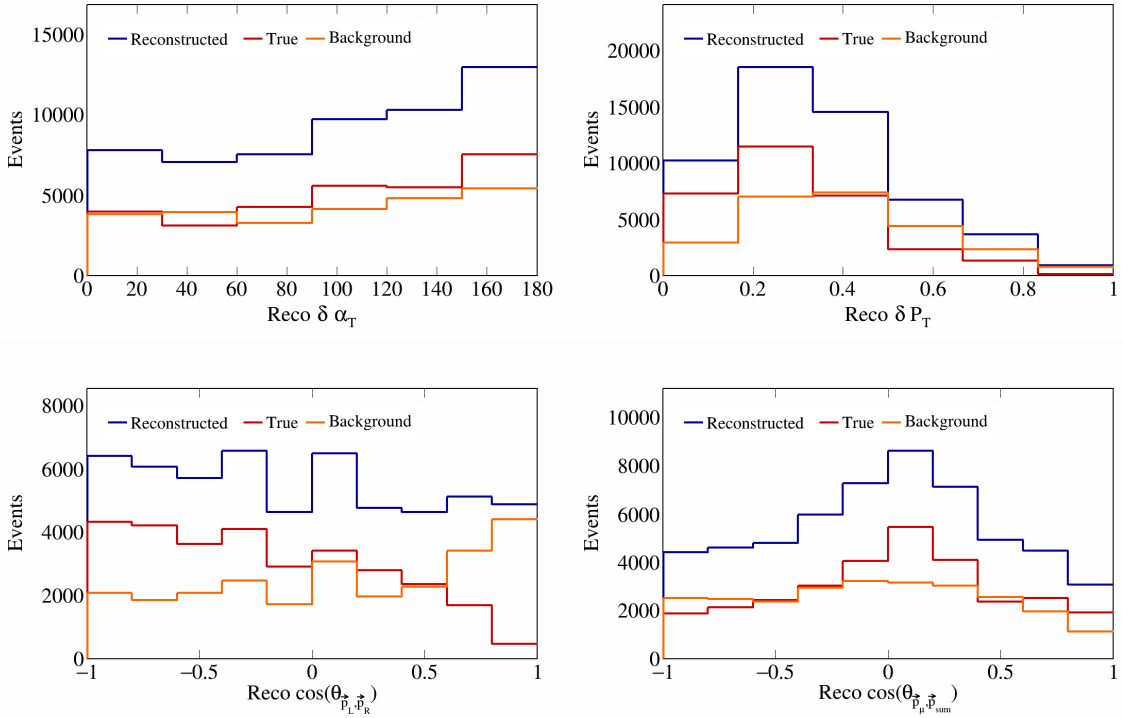


Figure 13: Vector opening angles and transverse momentum for SBND data.

and multisim. For the former, we consider a 1σ variation of the affected parameters, and in the latter we consider one hundred universes, each with a random variation picked from a Gaussian distribution between 0σ and 1σ . From these variations, we compute the covariance matrix as

$$E_{i,j} = \frac{1}{N_{\text{Univ}}} \sum_{s=1}^{N_{\text{Univ}}} (\tilde{\sigma}_i^{\text{Var},s} - \tilde{\sigma}_i^{\text{CV}})(\tilde{\sigma}_j^{\text{Var},s} - \tilde{\sigma}_j^{\text{CV}}) \quad (7)$$

where $\tilde{\sigma}_i^{\text{Var},s}$ represents the variation cross section of the variable in the i -th bin in the s -th universe, and $\tilde{\sigma}_i^{\text{CV}}$ is the central value (without any variation) of the cross section in the i -th bin. Then, the fractional covariance matrix is defined as

$$F_{i,j} = \frac{E_{i,j}}{\tilde{\sigma}_i^{\text{CV}} \tilde{\sigma}_j^{\text{CV}}}. \quad (8)$$

And the correlation matrix is defined as

$$\rho_{i,j} = \frac{E_{i,j}}{\sqrt{E_{i,i} E_{j,j}}}. \quad (9)$$

In the case of a multisigma systematic, $N_{\text{Univ}} = 1$, and for a multisim systematic, $N_{\text{Univ}} = 100$. The plots for all the individual cross sectional systematics are shown in Appendix 5.1. There are a few systematics that are currently crashing when trying to produce all plots. This are:

- MINERVAq0q3Weighting_SBND_v1_Mnv2p2hGaussEnhancement
- MiscInteractionSysts_SBND_v1_nuenuebar_xsec_ratio
- MiscInteractionSysts_SBND_v1_nuenumu_xsec_ratio
- NOvAStyleNonResPionNorm_SBND_v1_NR_nu_np_CC_1Pi

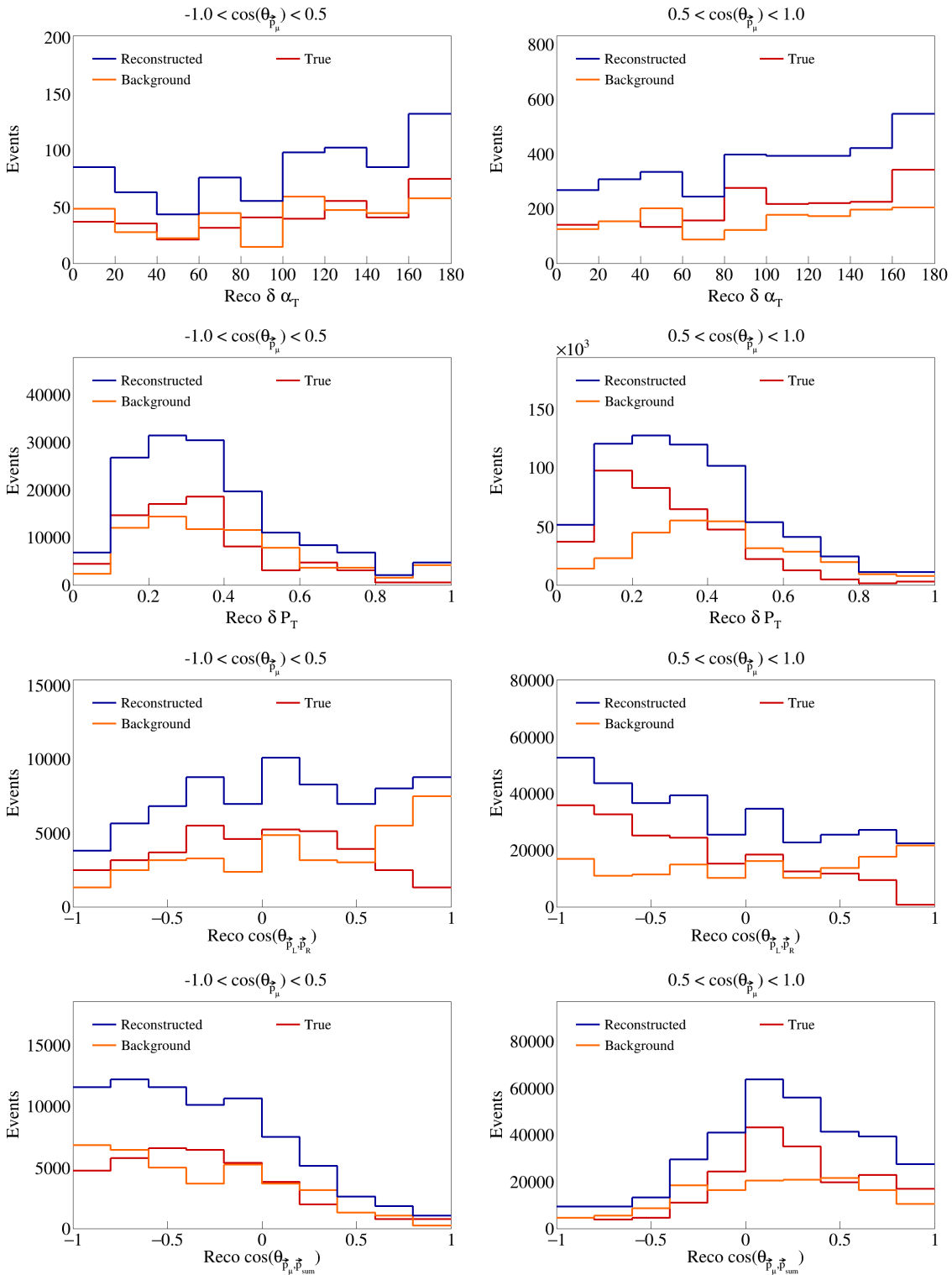


Figure 14: Sliced double differential plots for SBND events.

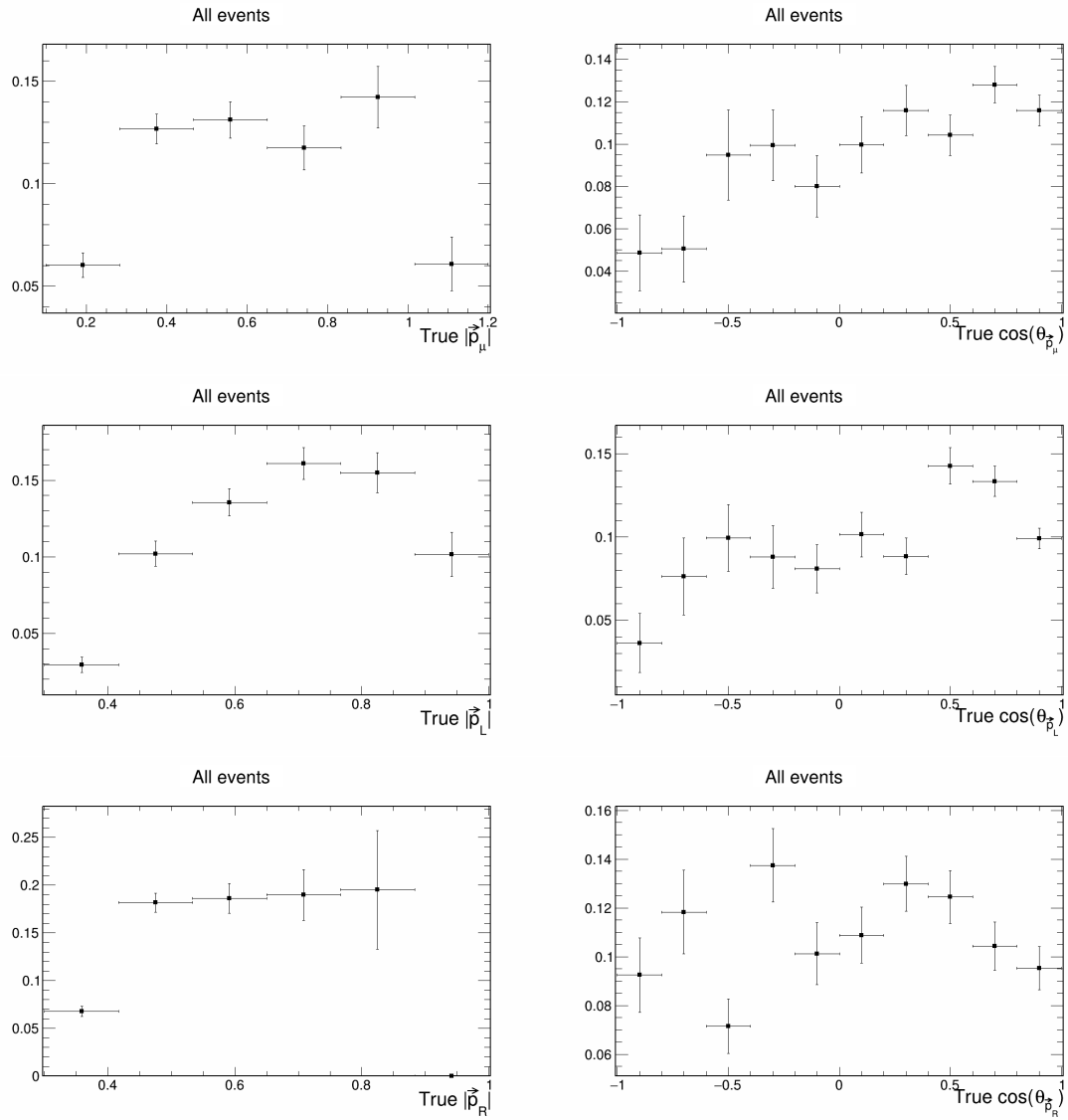


Figure 15: Signal efficiency plots for single differential vector directions and magnitudes.

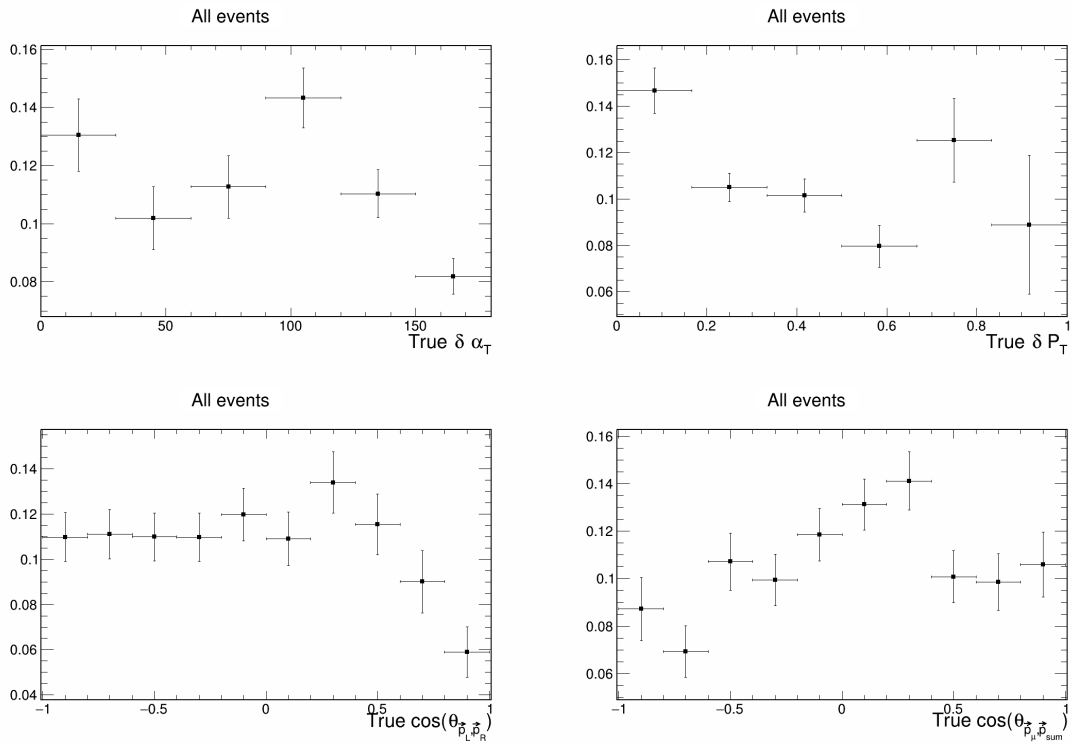


Figure 16: Signal efficiency plots for single differential vector opening angles and transverse momentum.

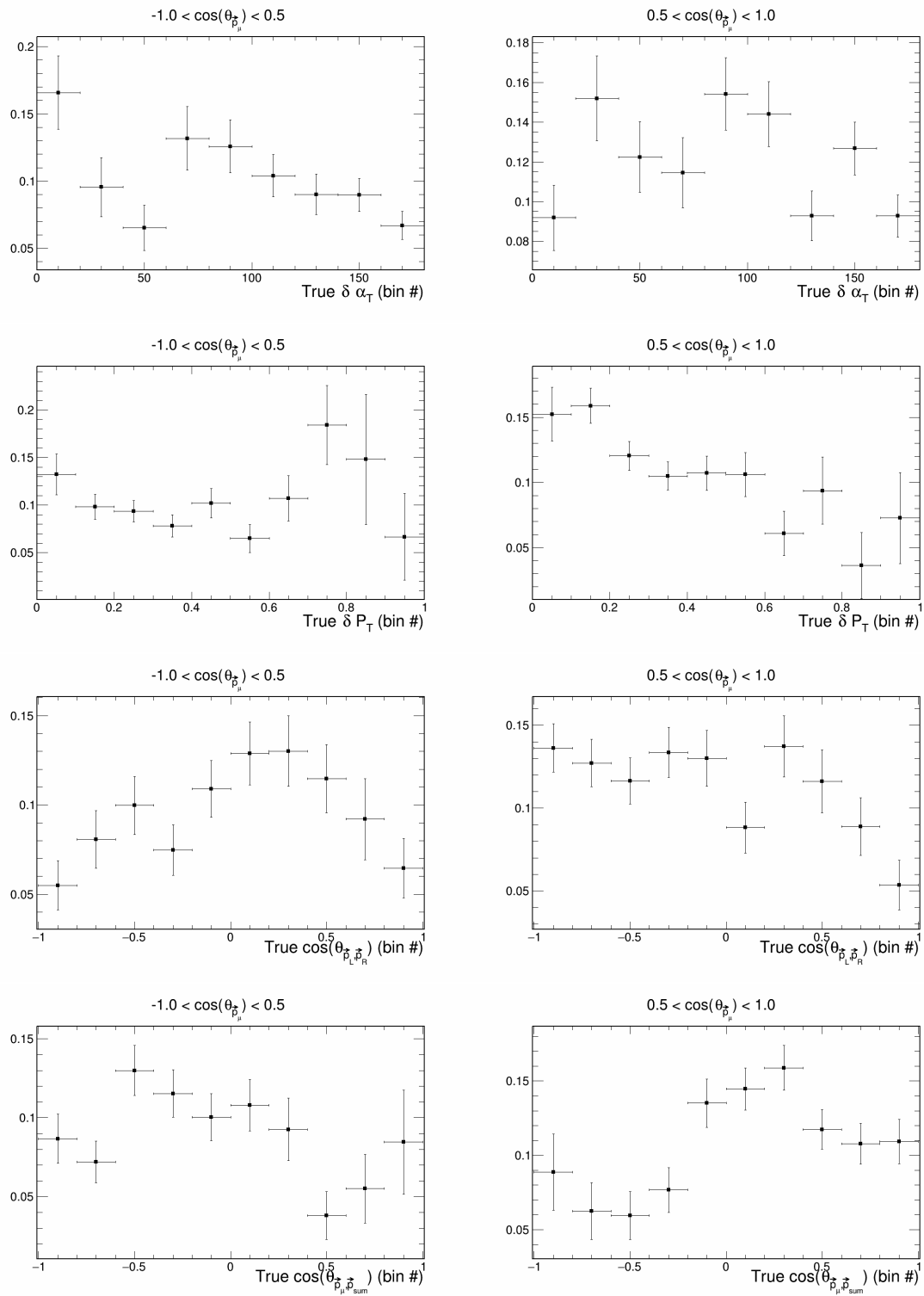


Figure 17: Signal efficiency plots for double differential variables.

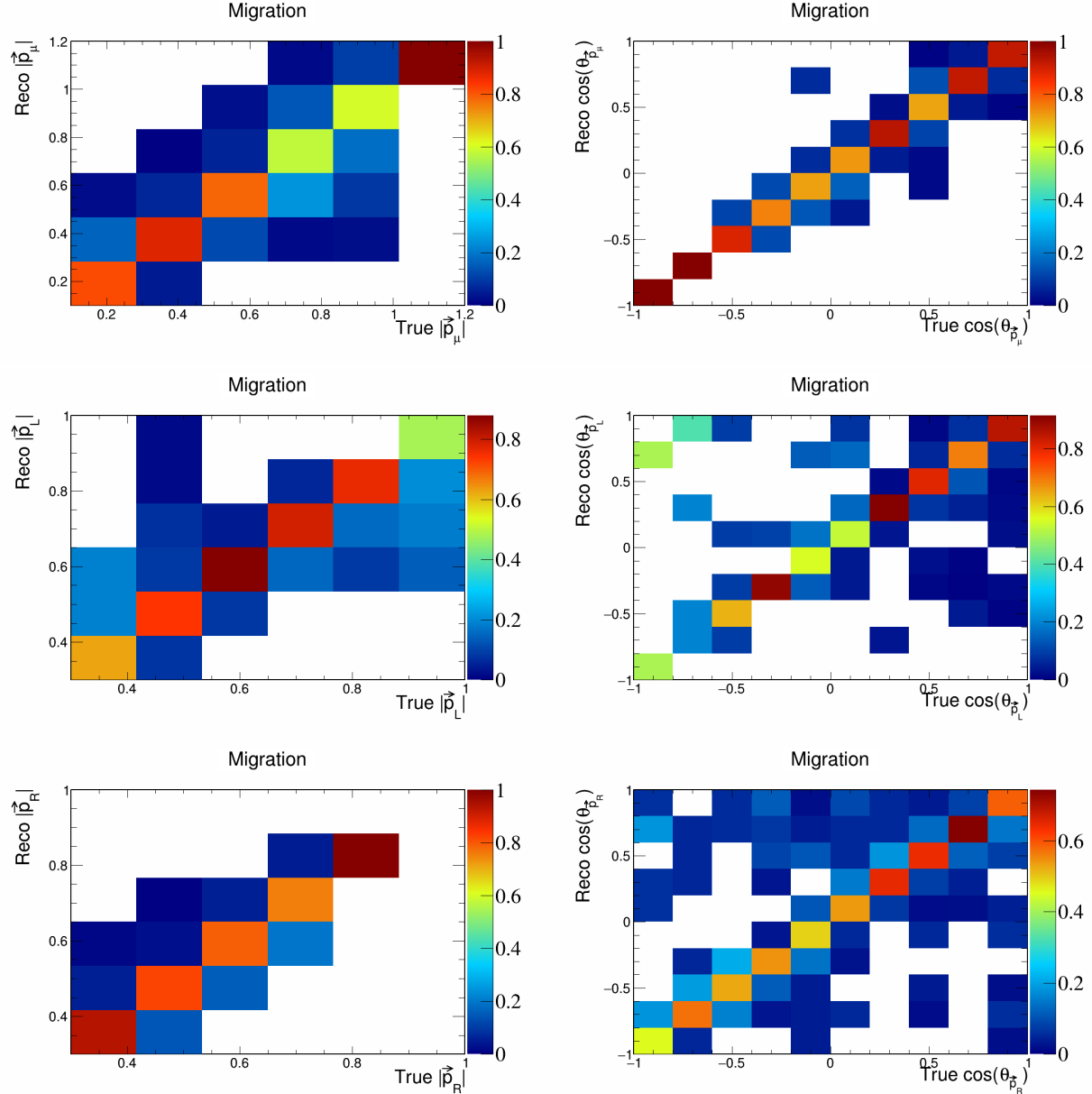


Figure 18: Migration matrices for signal differential vector directions and magnitudes.

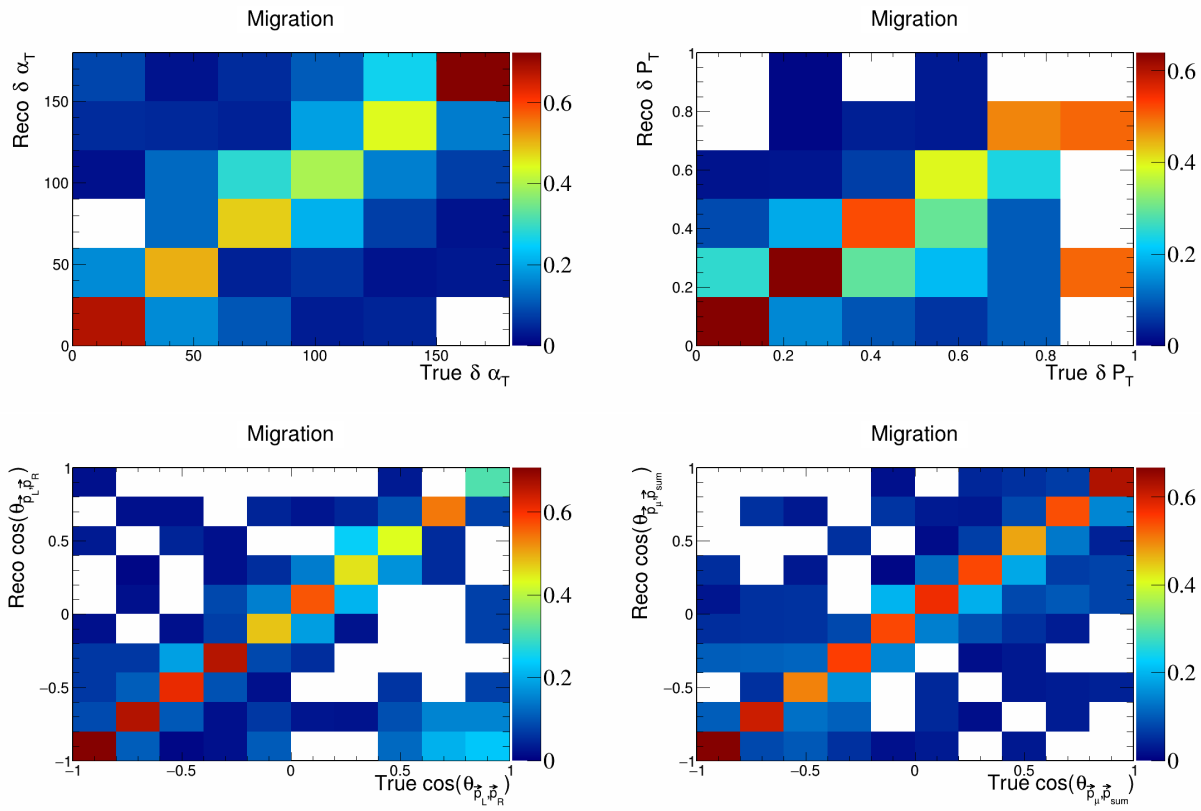


Figure 19: Migration matrices for signal differential vector opening angles and transverse momentum.

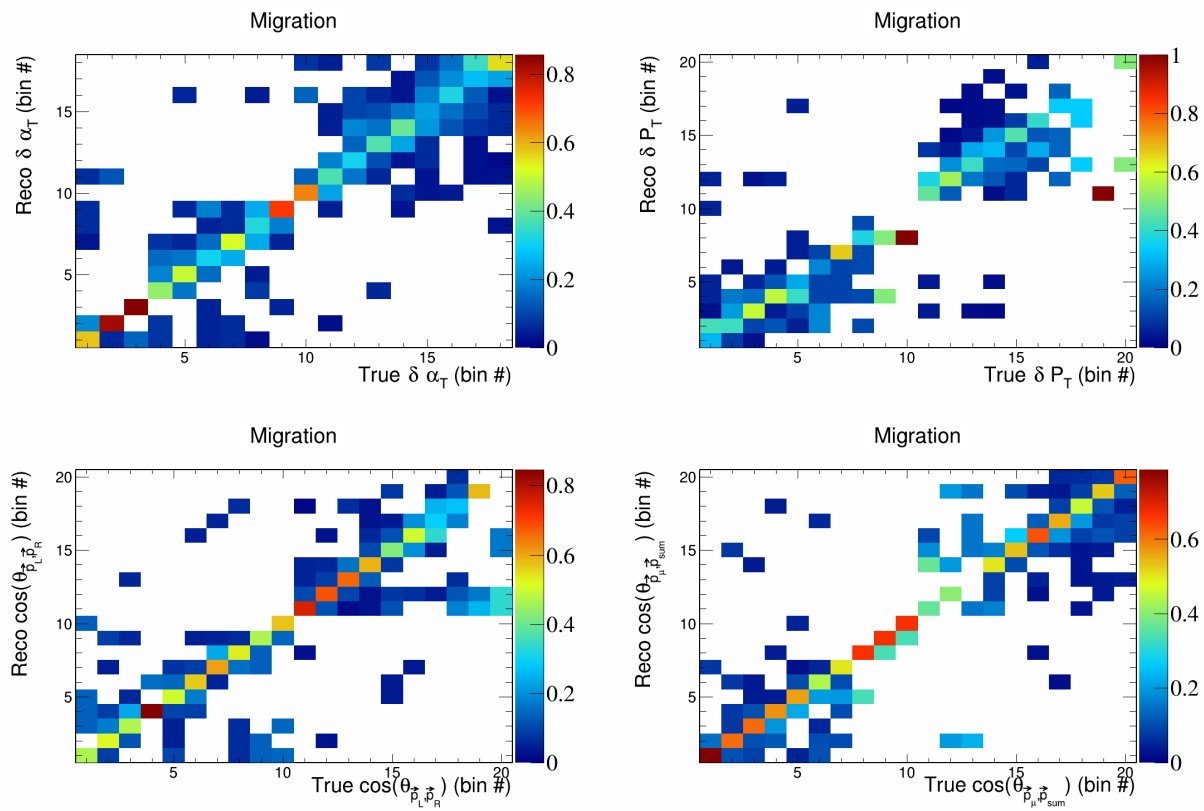


Figure 20: Migration matrices for double differential variables.

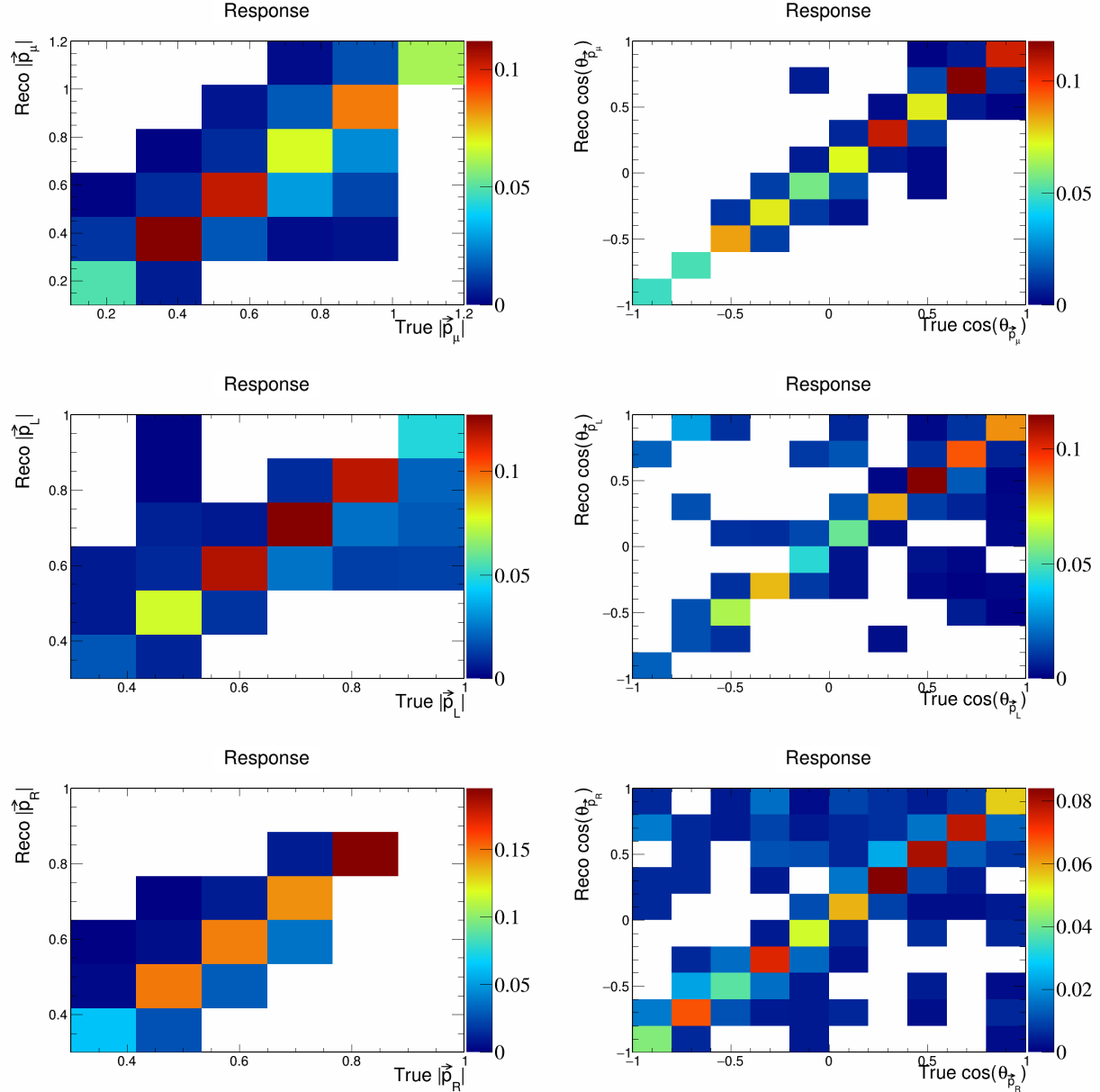


Figure 21: Response matrices for signal differential vector directions and magnitudes.

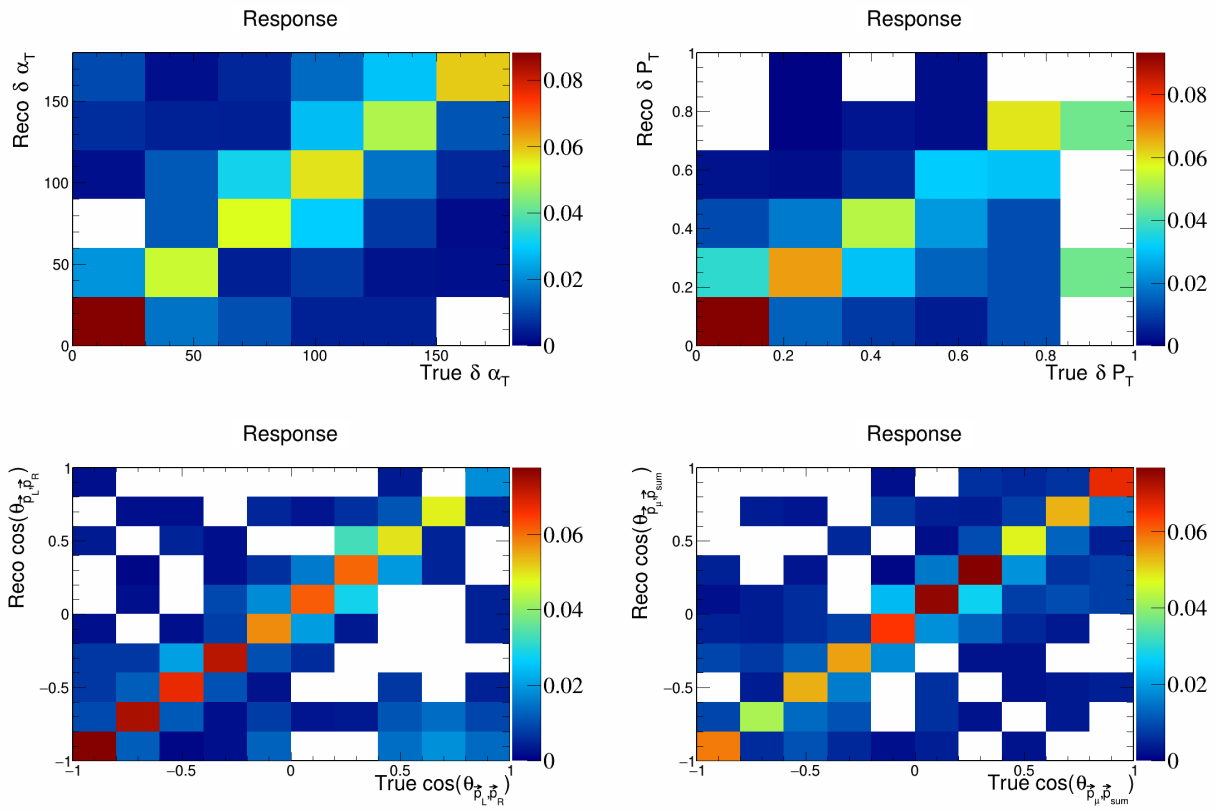


Figure 22: Response matrices for signal differential vector opening angles and transverse momentum.

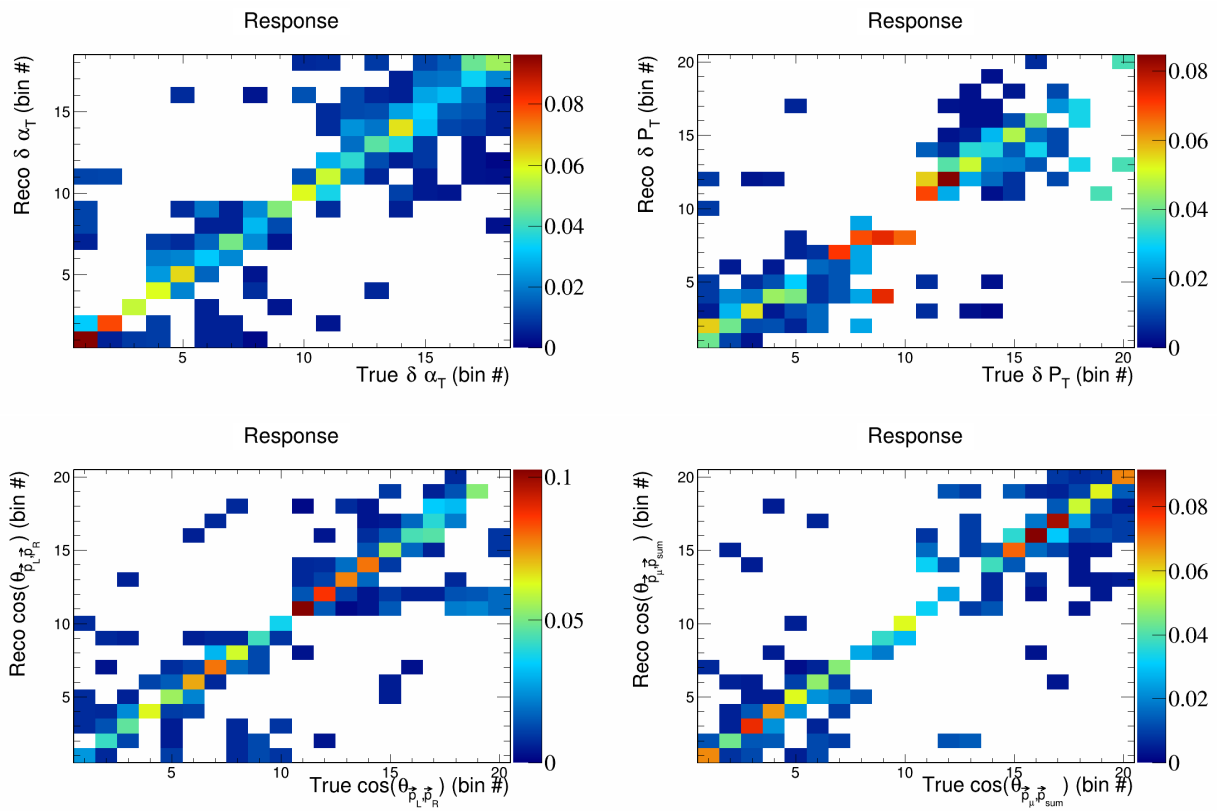


Figure 23: Response matrices for double differential variables.

₁₆₁ **3 Closure test**

₁₆₂ To ensure that the unfolding techniques that we will implement work correctly, we perform a closure test,
₁₆₃ meaning that we will perform the unfolding on simulated true signal events and check that the unfolded
₁₆₄ data matches the true signal data with added smearing. We can see that the plots that perform this test
₁₆₅ in Figure 24 and Figure 25. We also note that the overall shape and magnitude of our histograms match
₁₆₆ previously reported MicroBooNE analyses. **TODO: stop using dummy covariance matrices.**

₁₆₇ **4 Cross-section results**

₁₆₈ Placeholder.

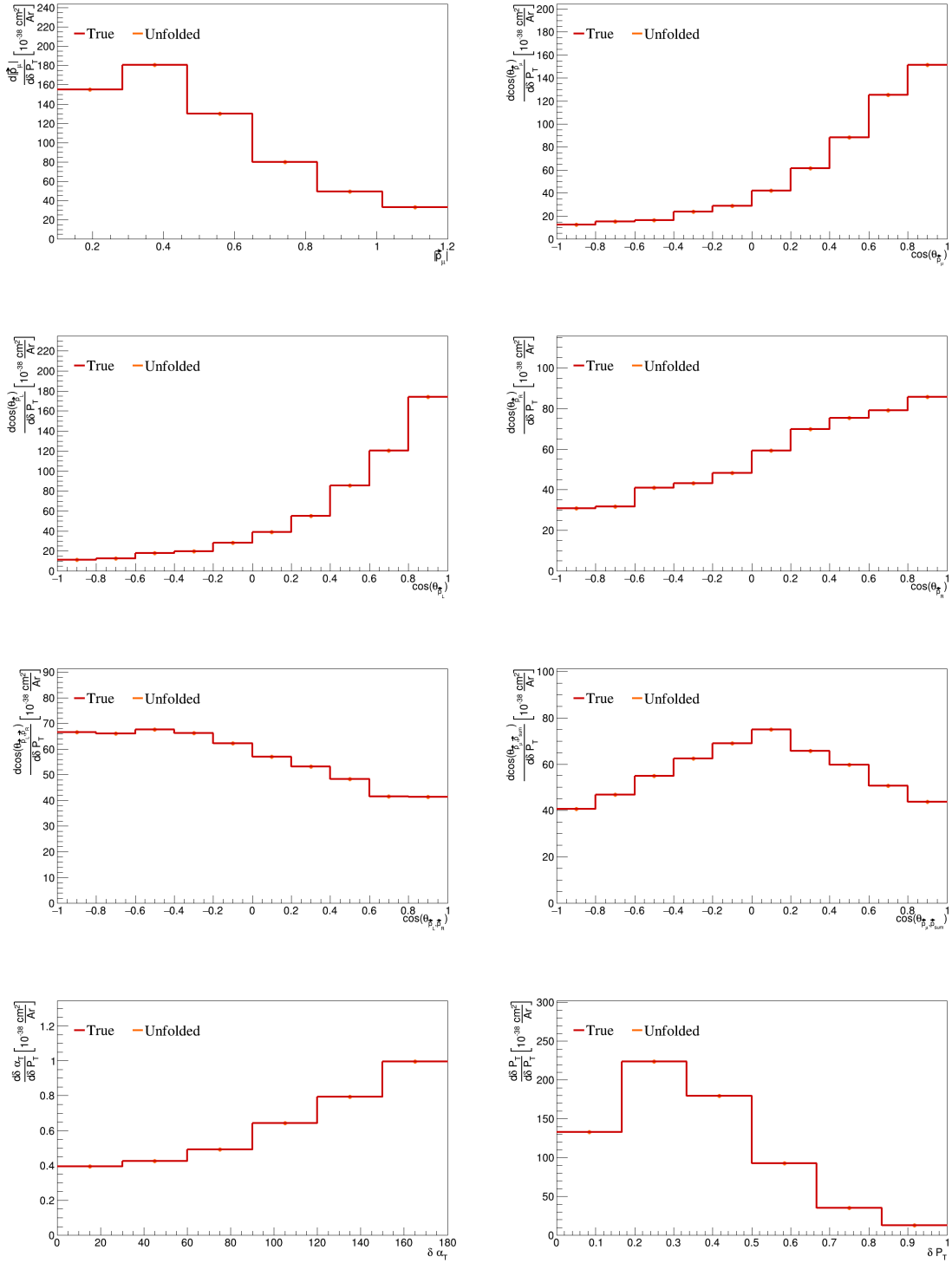


Figure 24: Closure test single differential plots.

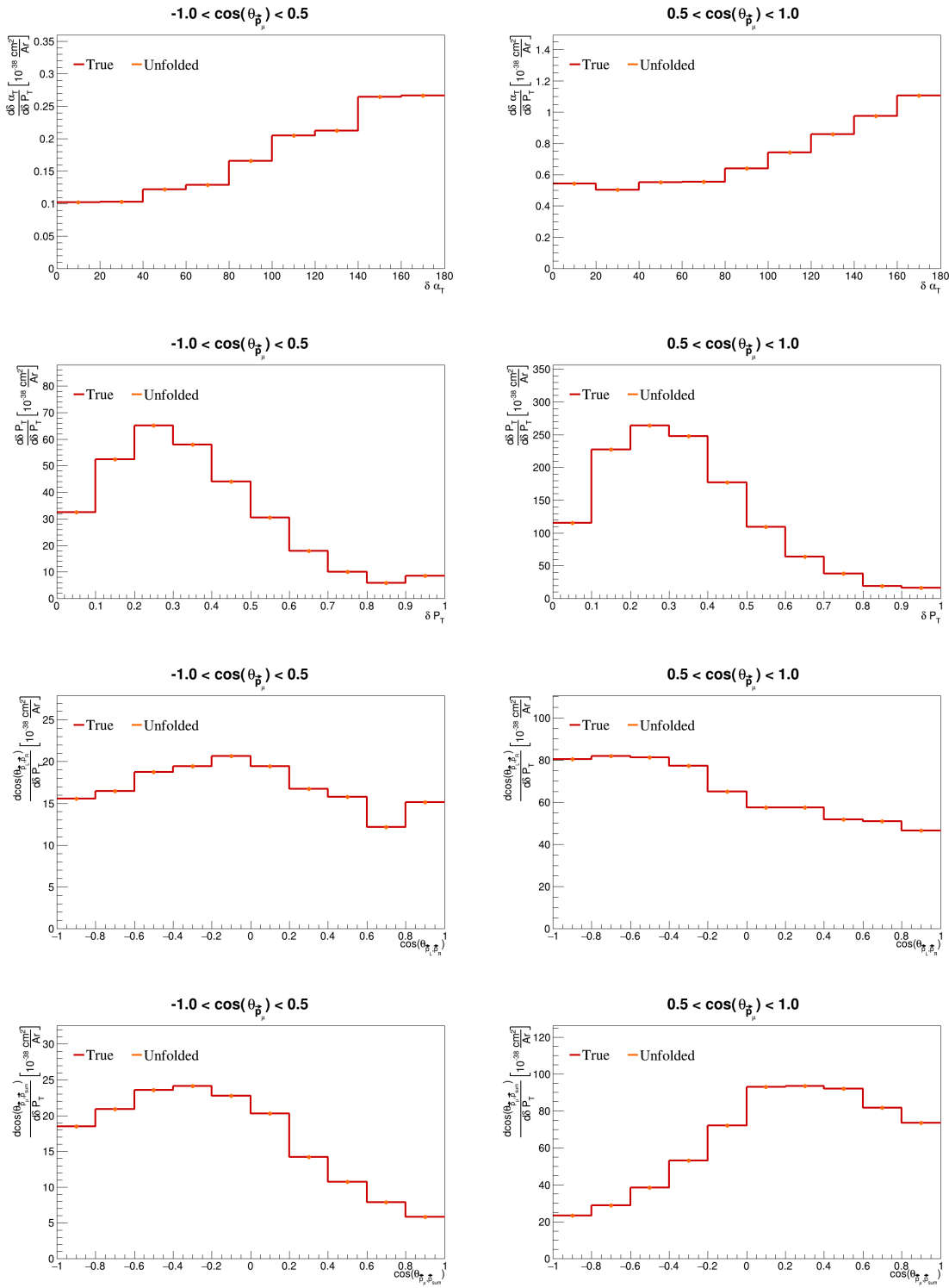


Figure 25: Closure test double differential plots.

169 **5 Appendices**

170 **5.1 Cross section systematics**

171 In this appendix, the variations, covariance matrices, fractional covariance matrices, and correlation matrices
 172 are plotted for all of the cross section systematics and variables.

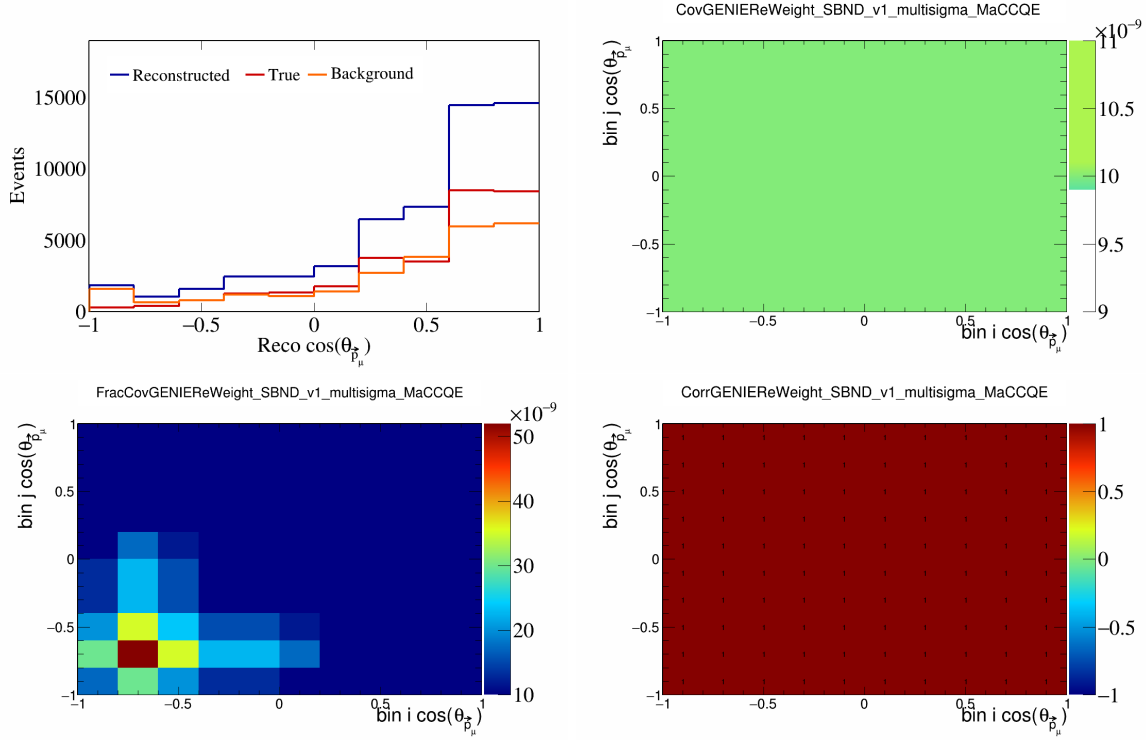


Figure 26: GenieMaCCQE variations for $\cos(\theta_{\vec{p}_\mu})$.

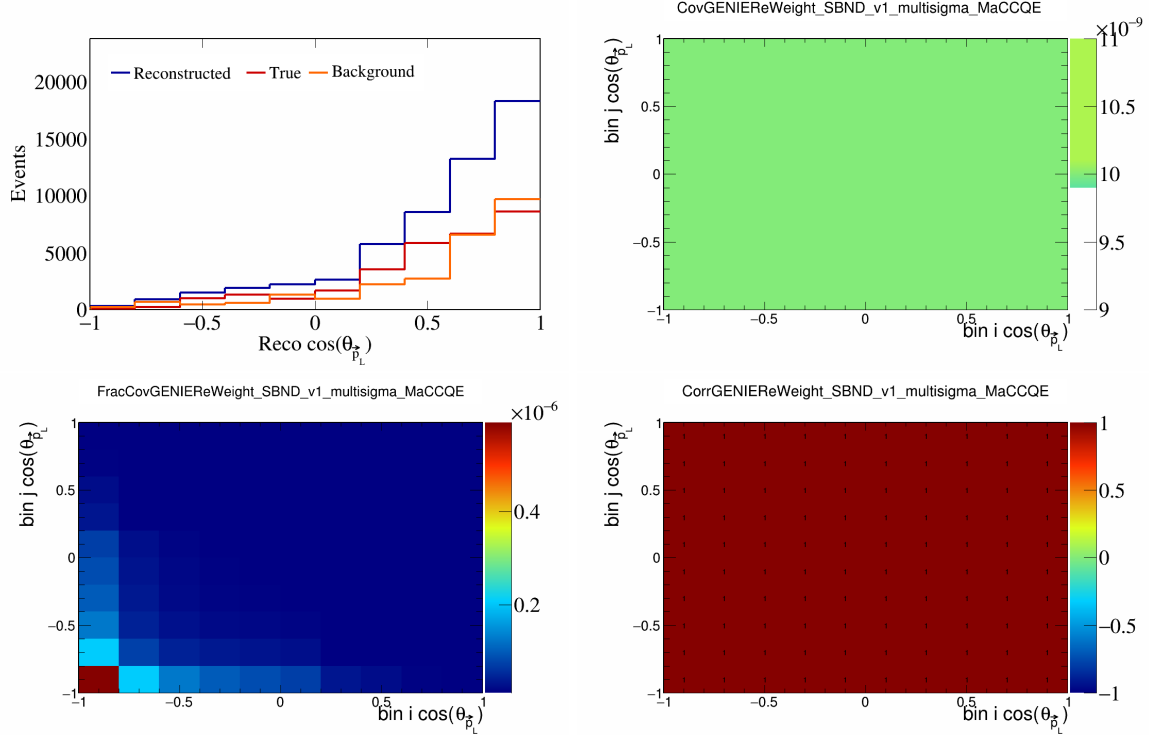


Figure 27: GenieMaCCQE variations for $\cos(\theta_{\vec{p}_L})$.

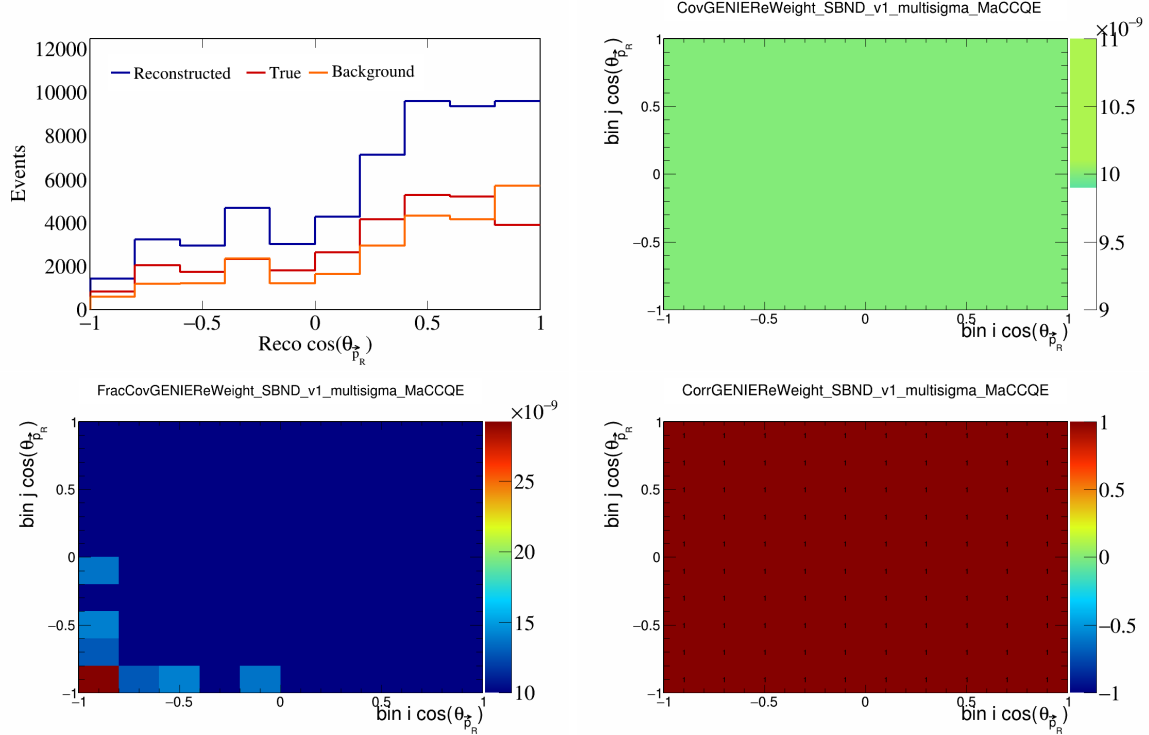


Figure 28: GenieMaCCQE variations for $\cos(\theta_{\vec{p}_R})$.

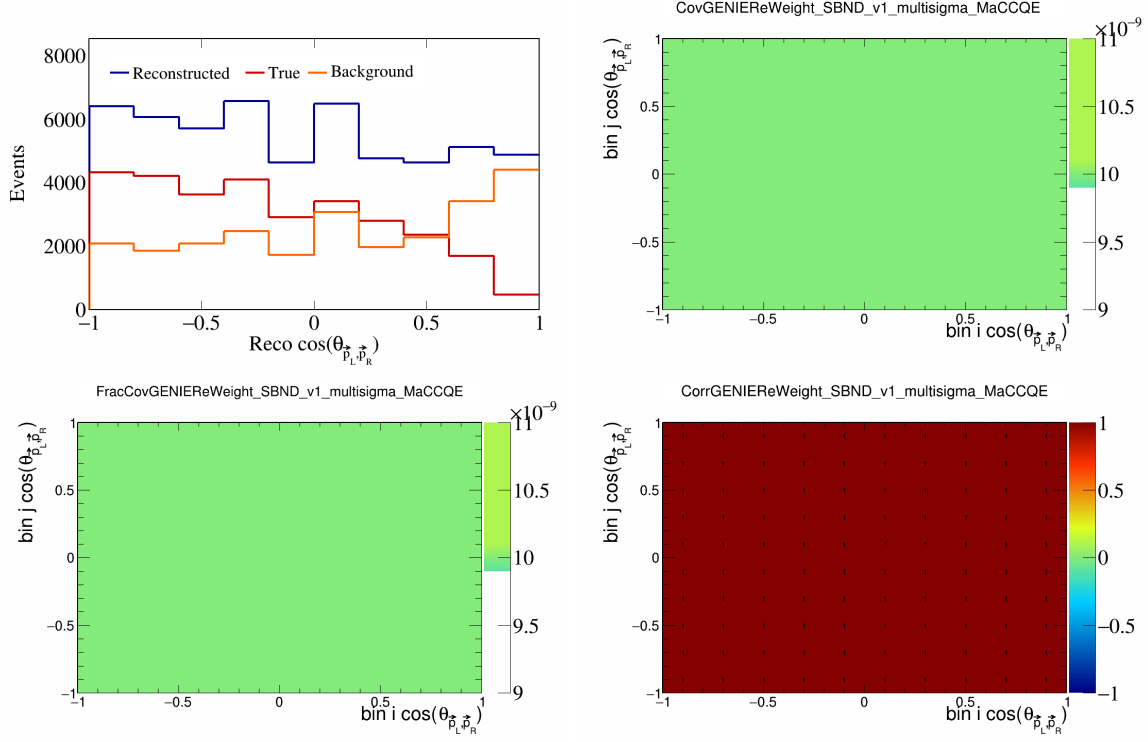


Figure 29: GenieMaCCQE variations for $\cos(\theta_{\vec{p}_L, \vec{p}_R})$.

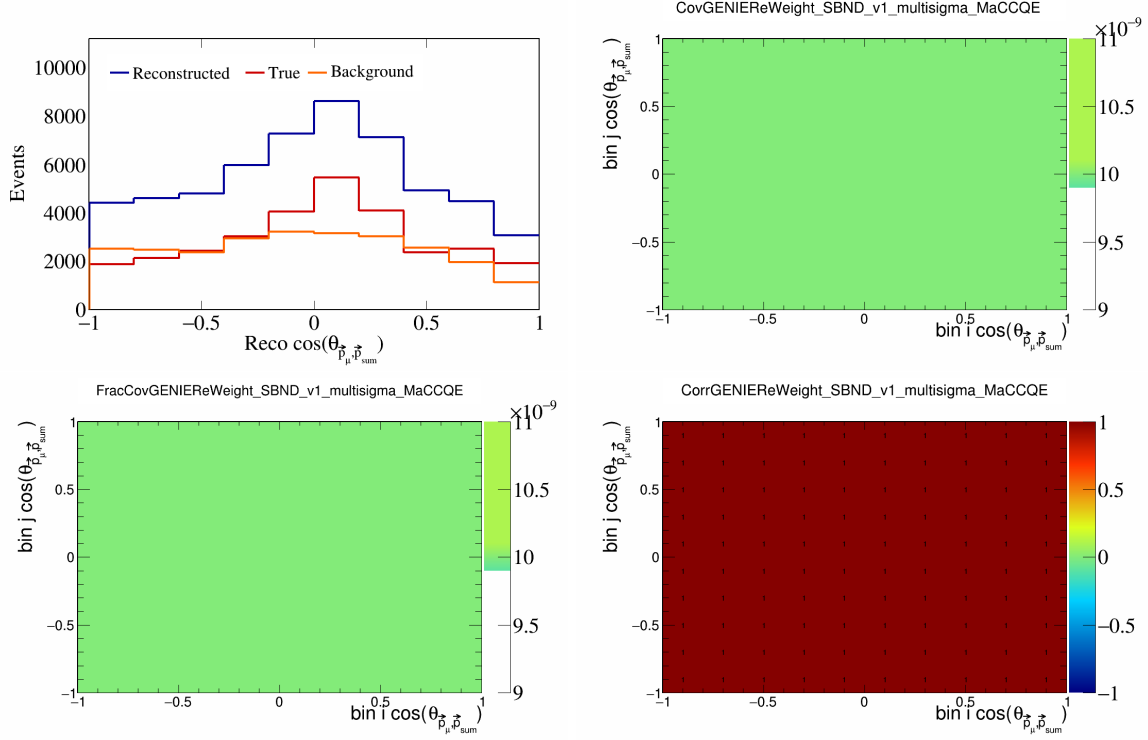


Figure 30: GenieMaCCQE variations for $\cos(\theta_{\vec{p}_\mu, \vec{p}_{\text{sum}}})$.

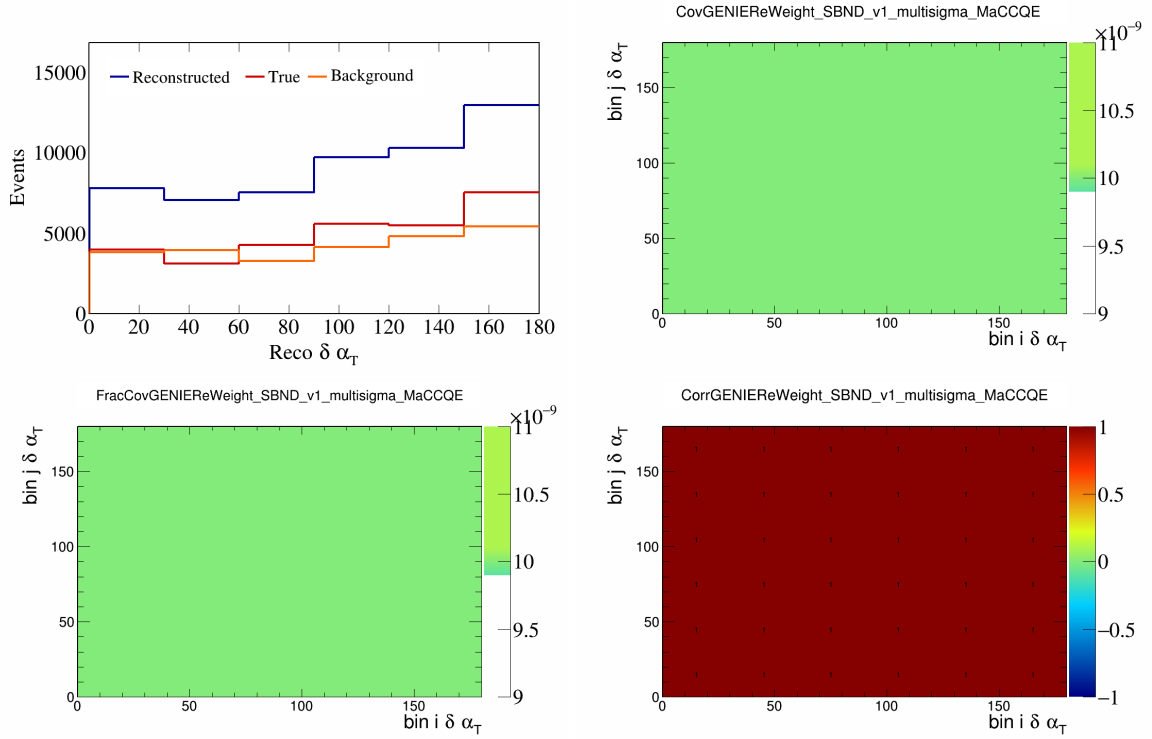


Figure 31: GenieMaCCQE variations for $\delta \alpha_T$.

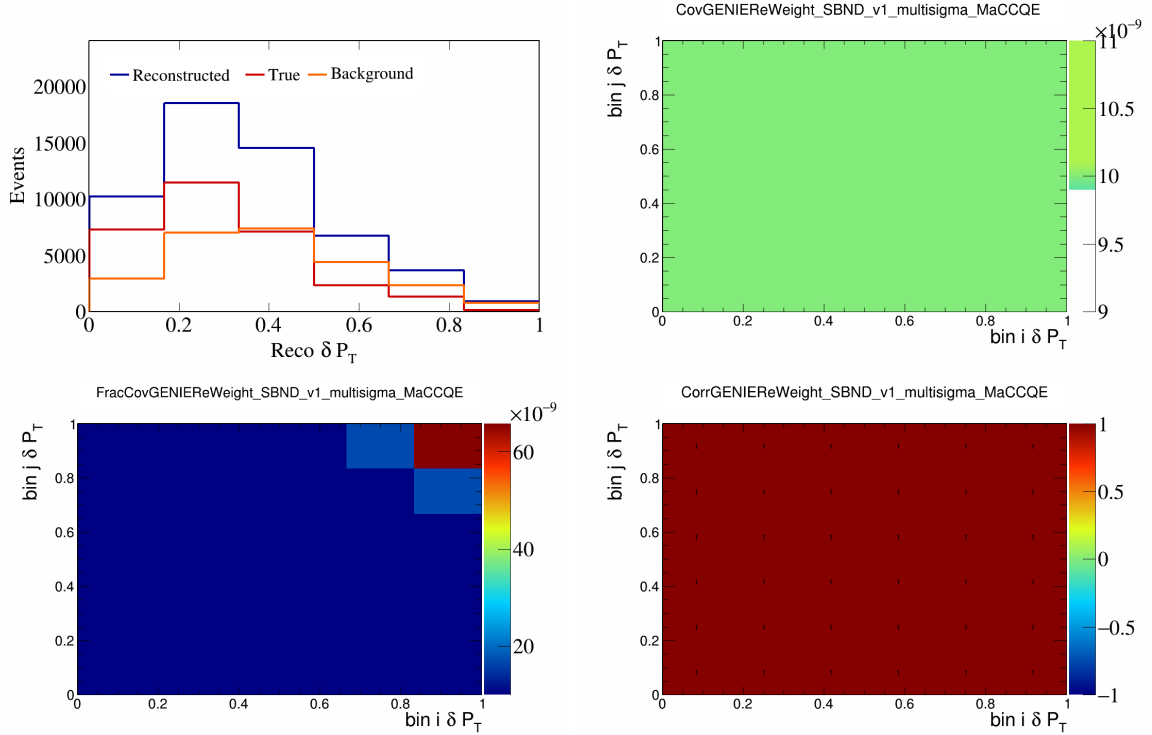


Figure 32: GenieMaCCQE variations for δP_T .

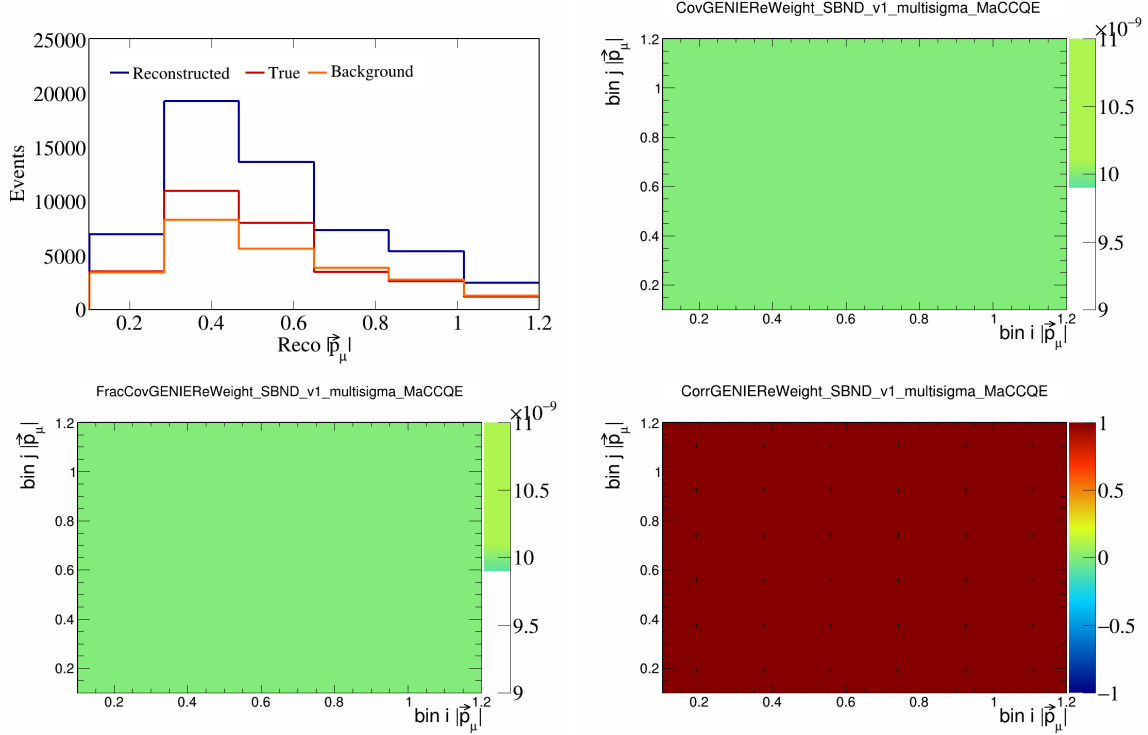


Figure 33: GenieMaCCQE variations for $|\vec{p}_\mu|$.

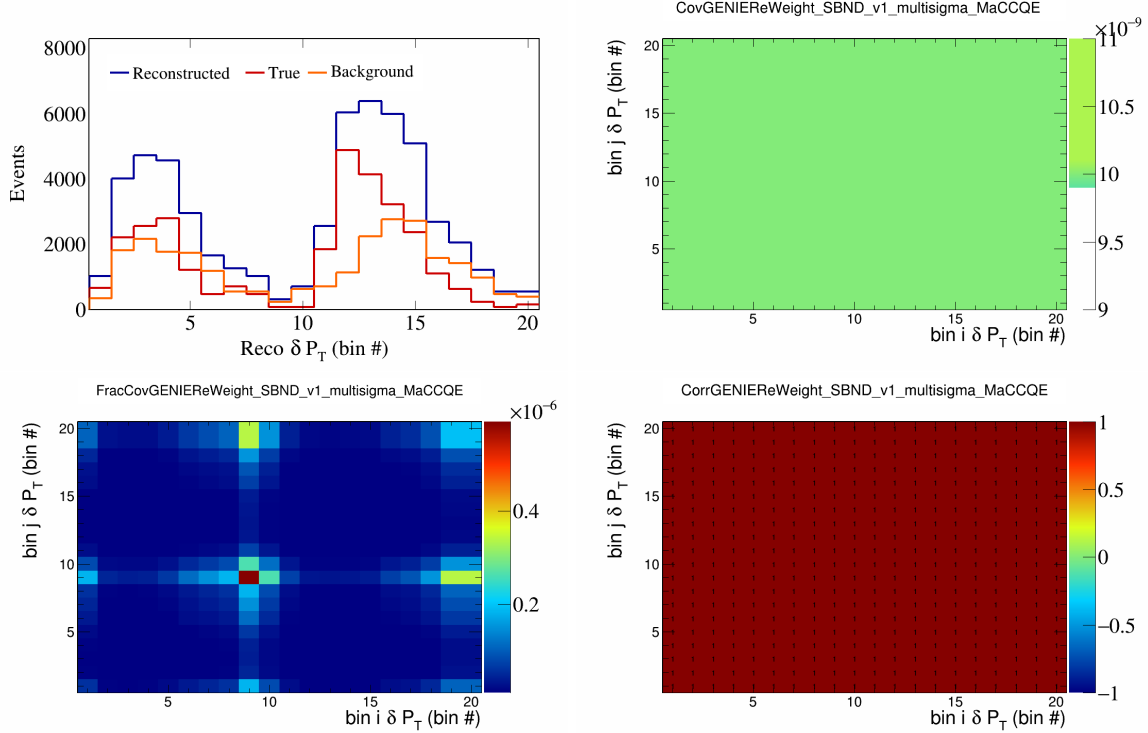


Figure 34: GenieMaCCQE variations for δP_T in $\cos(\theta_{\vec{p}_\mu})$.

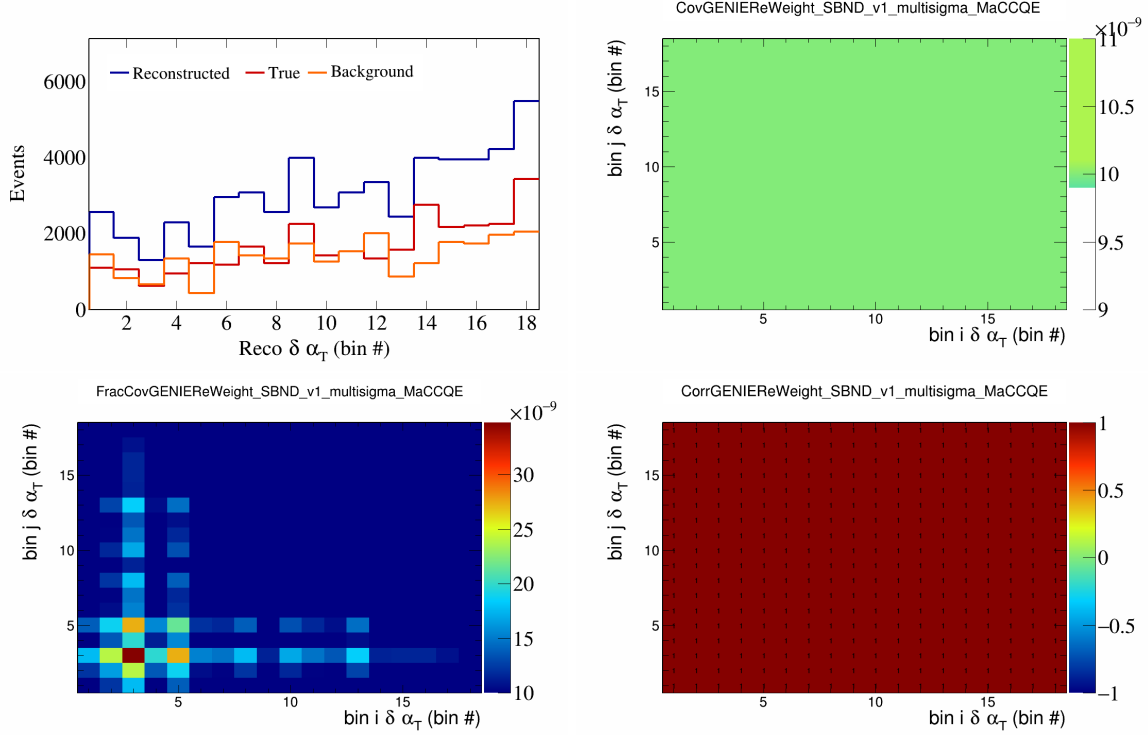


Figure 35: GenieMaCCQE variations for $\delta\alpha_T$ in $\cos(\theta_{\vec{p}_\mu})$.

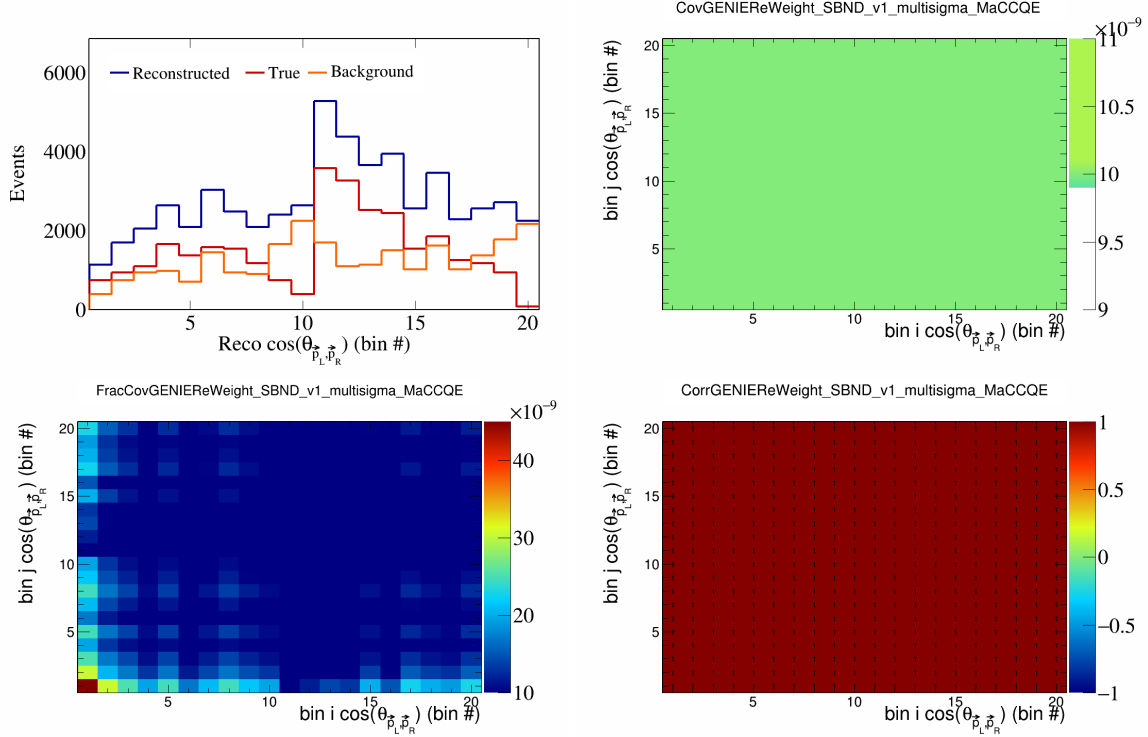


Figure 36: GenieMaCCQE variations for $\cos(\theta_{\vec{p}_L, \vec{p}_R})$ in $\cos(\theta_{\vec{p}_\mu})$.

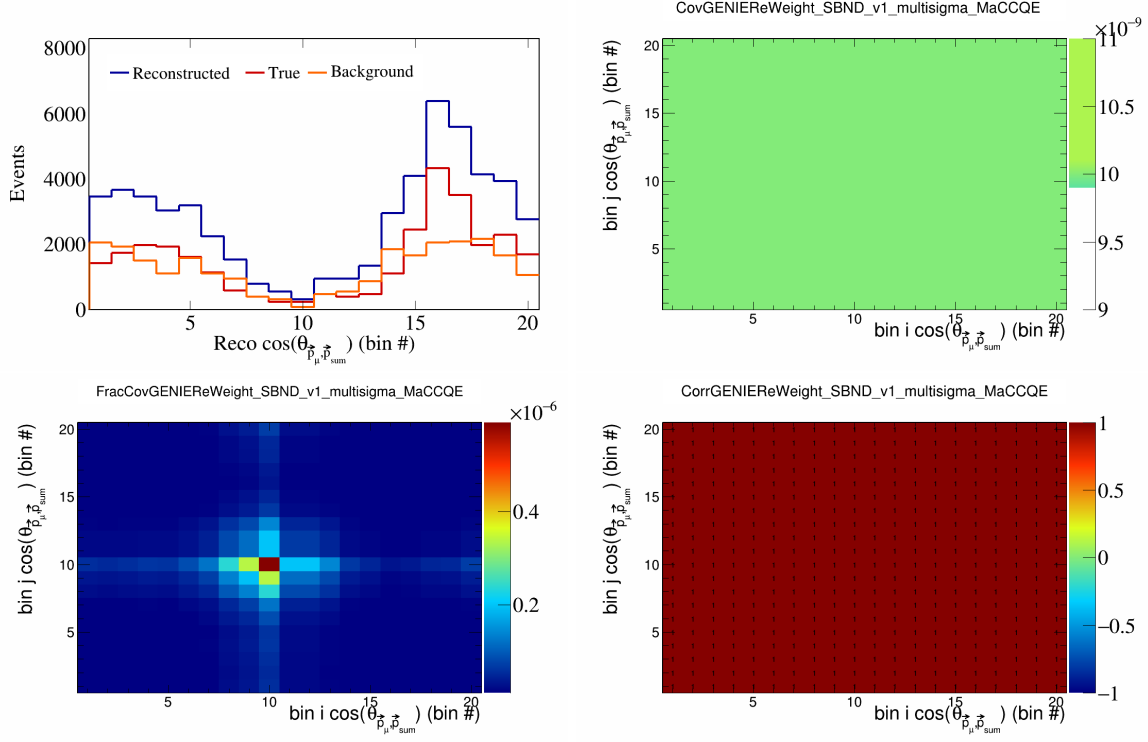


Figure 37: GenieMaCCQE variations for $\cos(\theta_{\vec{p}_\mu, \vec{p}_{\text{sum}}})$ in $\cos(\theta_{\vec{p}_\mu})$.

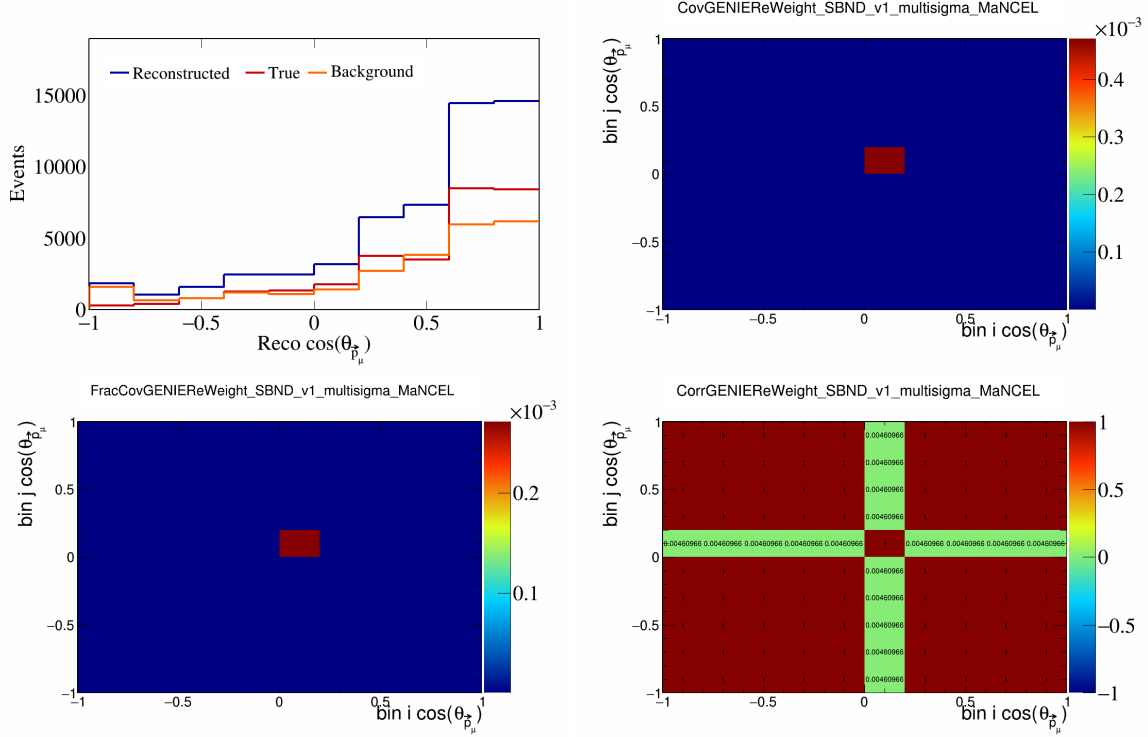


Figure 38: GenieMaNCEL variations for $\cos(\theta_{\vec{p}_\mu})$.

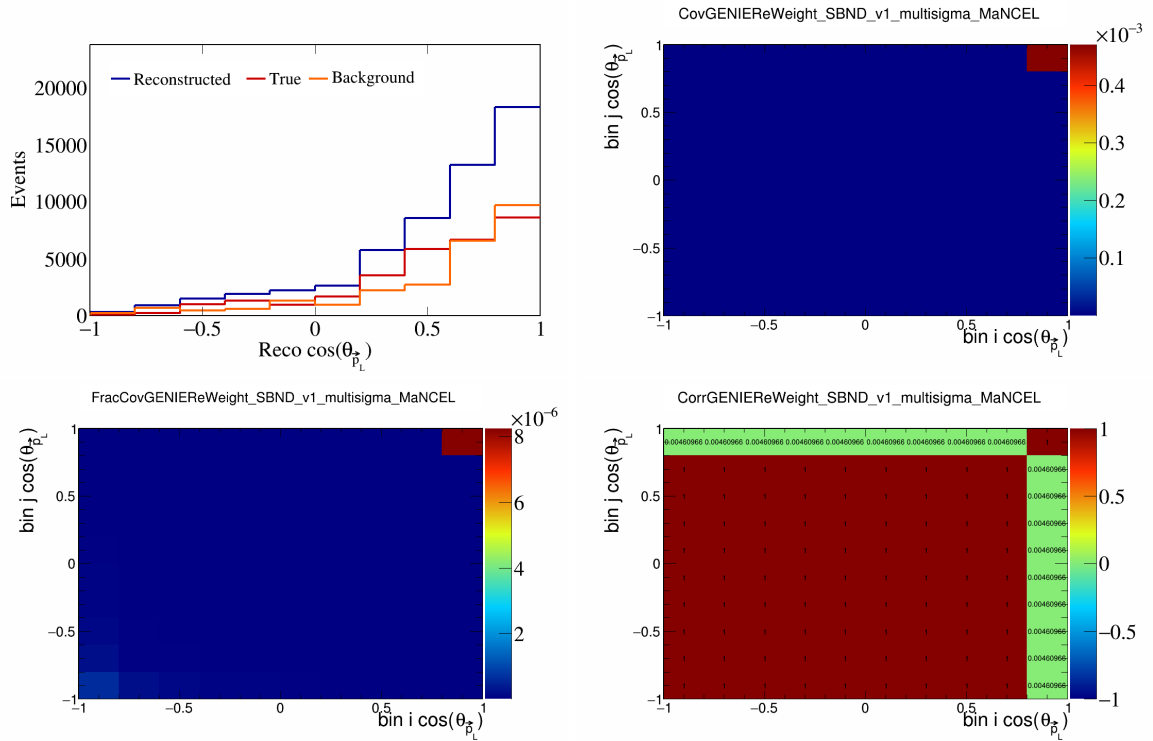


Figure 39: GenieMaNCEL variations for $\cos(\theta_{\vec{p}_L})$.

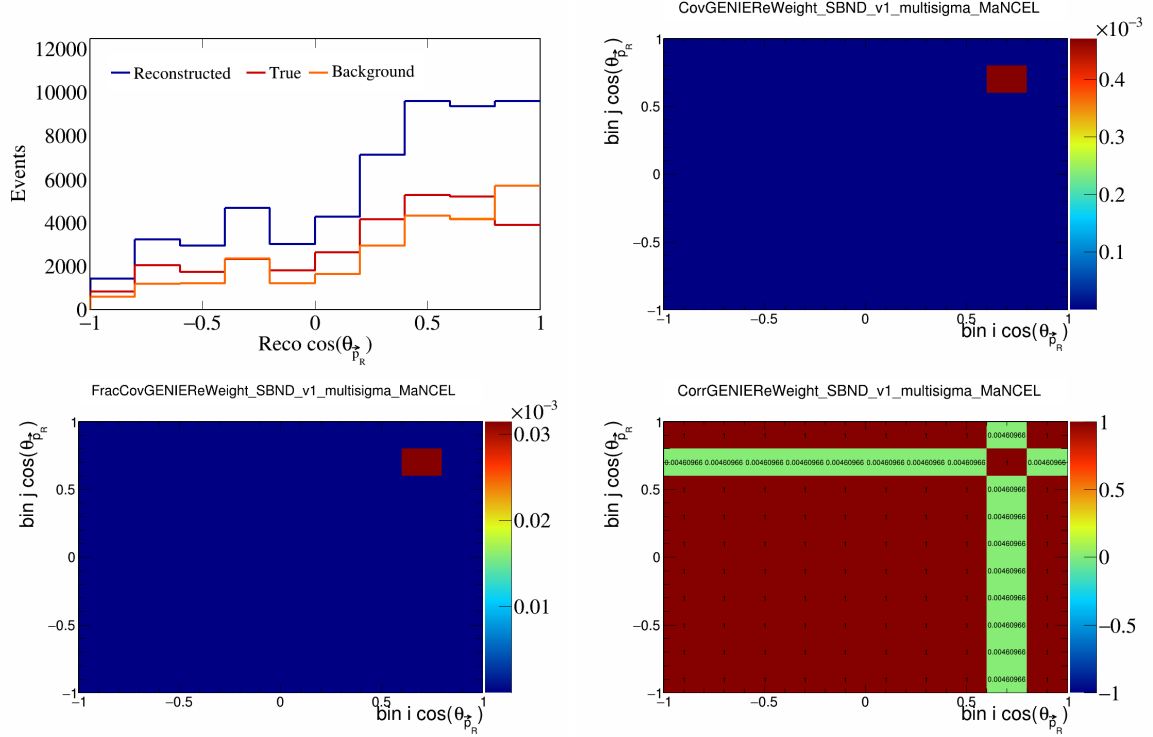


Figure 40: GenieMaNCEL variations for $\cos(\theta_{\vec{p}_R})$.

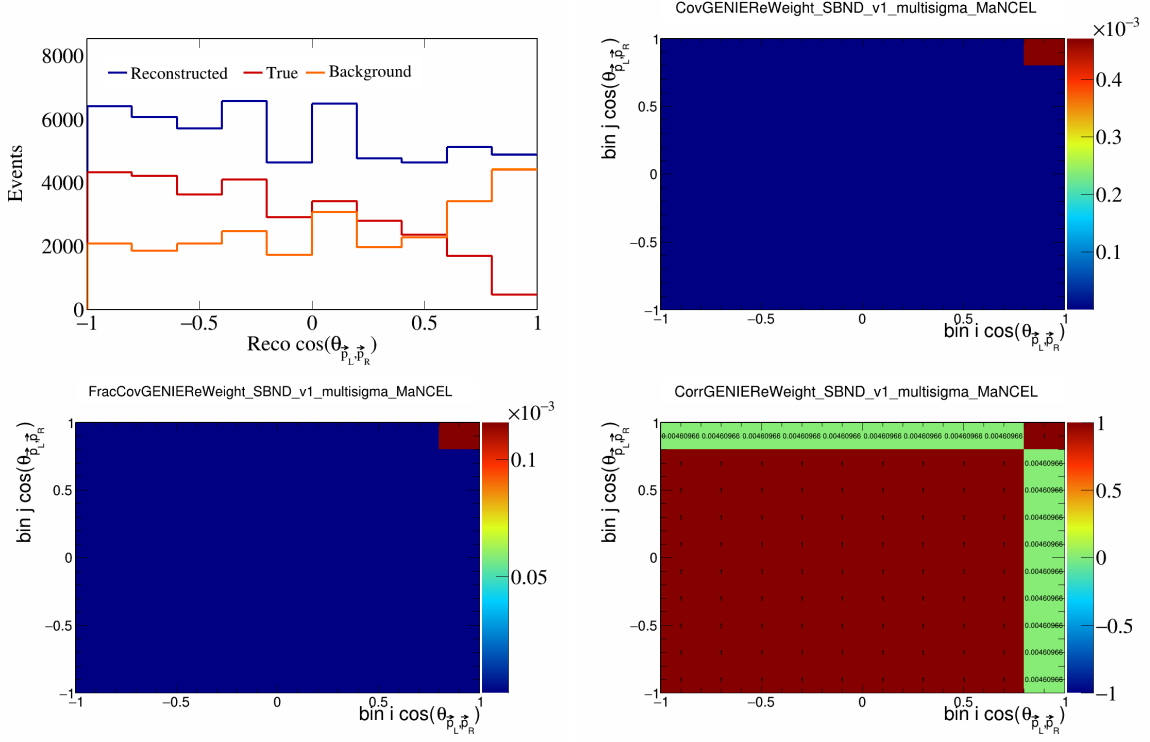


Figure 41: GenieMaNCEL variations for $\cos(\theta_{\vec{p}_L, \vec{p}_R})$.

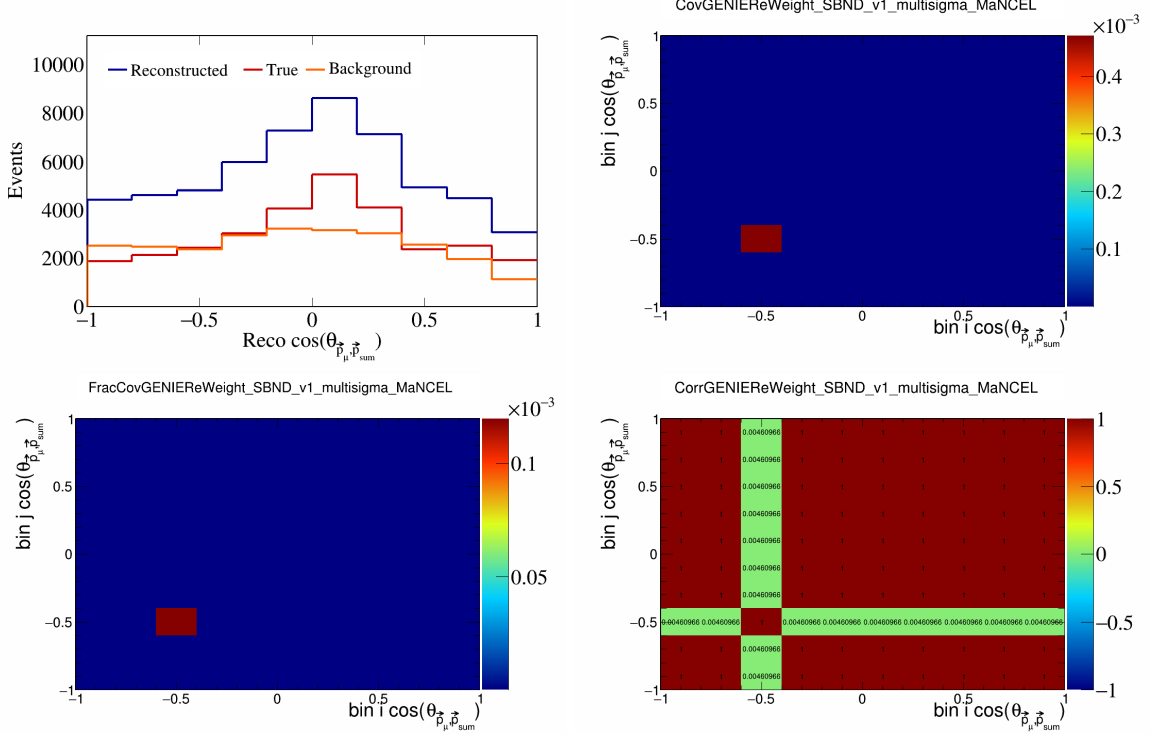


Figure 42: GenieMaNCEL variations for $\cos(\theta_{\vec{p}_\mu, \vec{p}_{\text{sum}}})$.

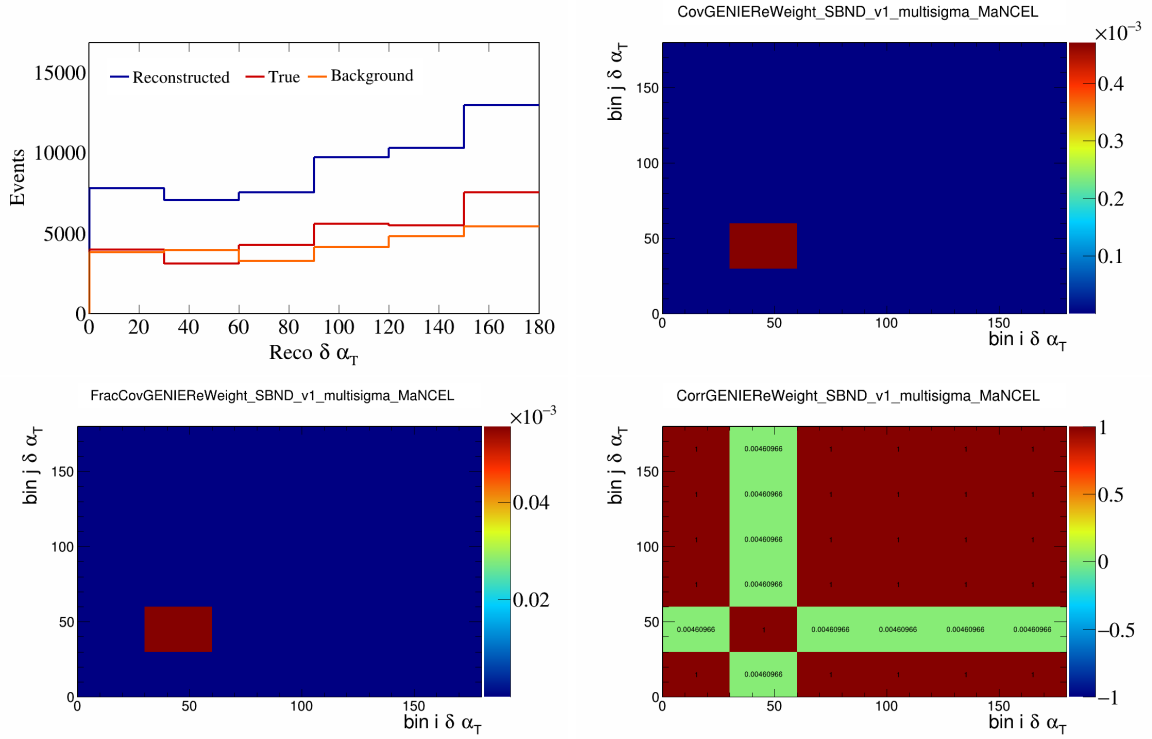


Figure 43: GenieMaNCEL variations for $\delta\alpha_T$.

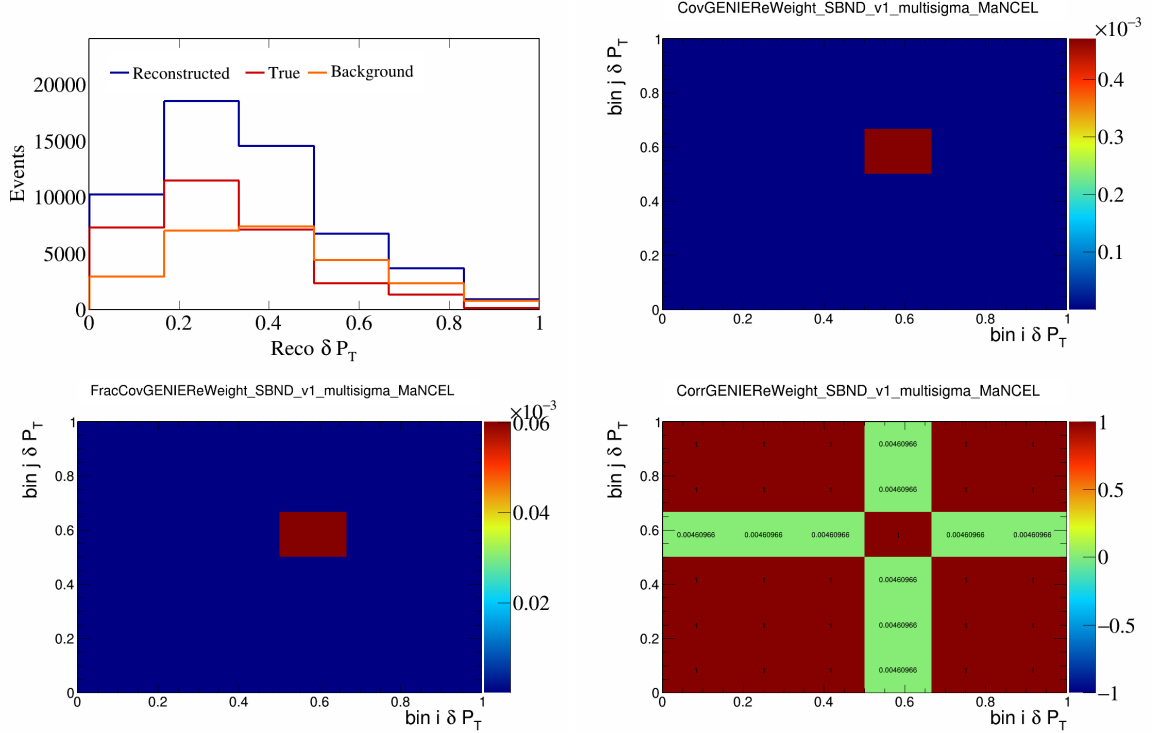


Figure 44: GenieMaNCEL variations for δP_T .

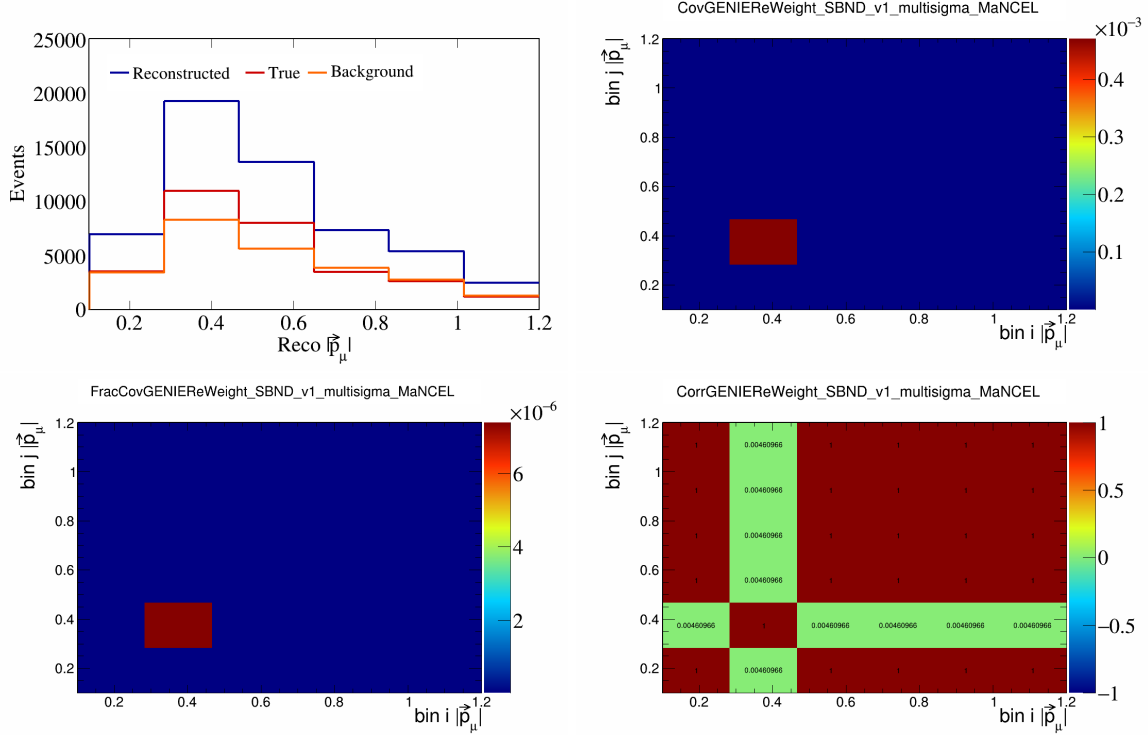


Figure 45: GenieMaNCEL variations for $|\vec{p}_\mu|$.

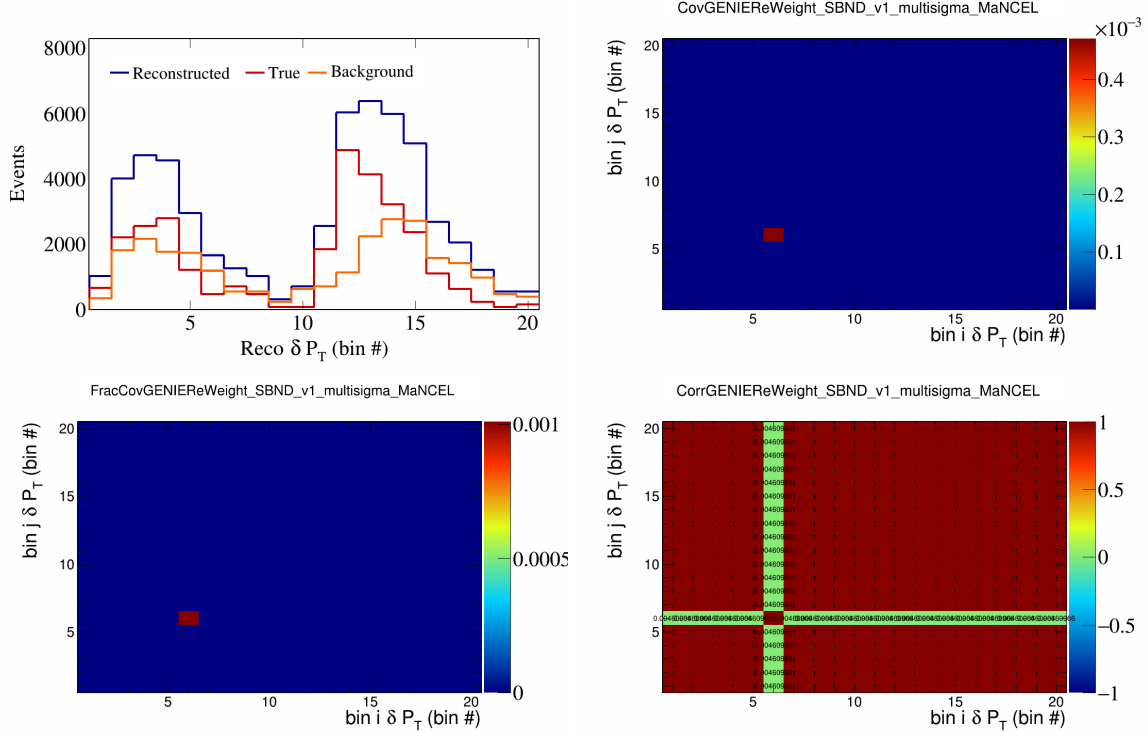


Figure 46: GenieMaNCEL variations for δP_T in $\cos(\theta_{\vec{p}_\mu})$.

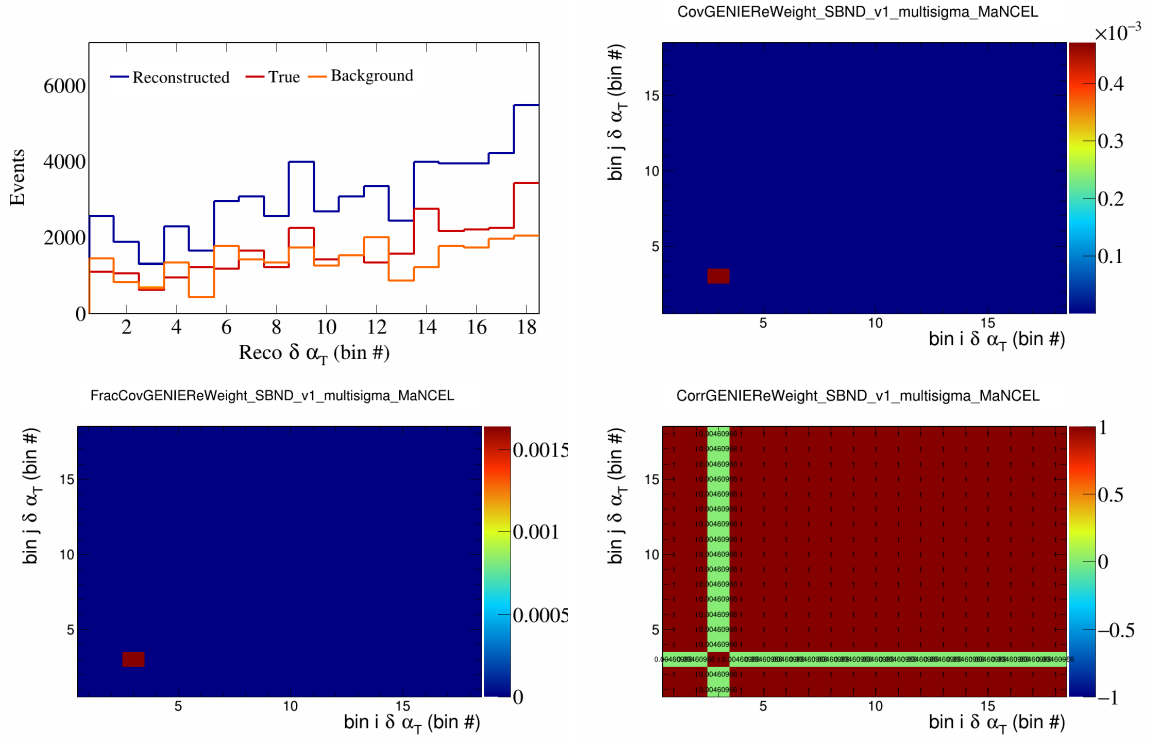


Figure 47: GenieMaNCEL variations for $\delta\alpha_T$ in $\cos(\theta_{\vec{p}_\mu})$.

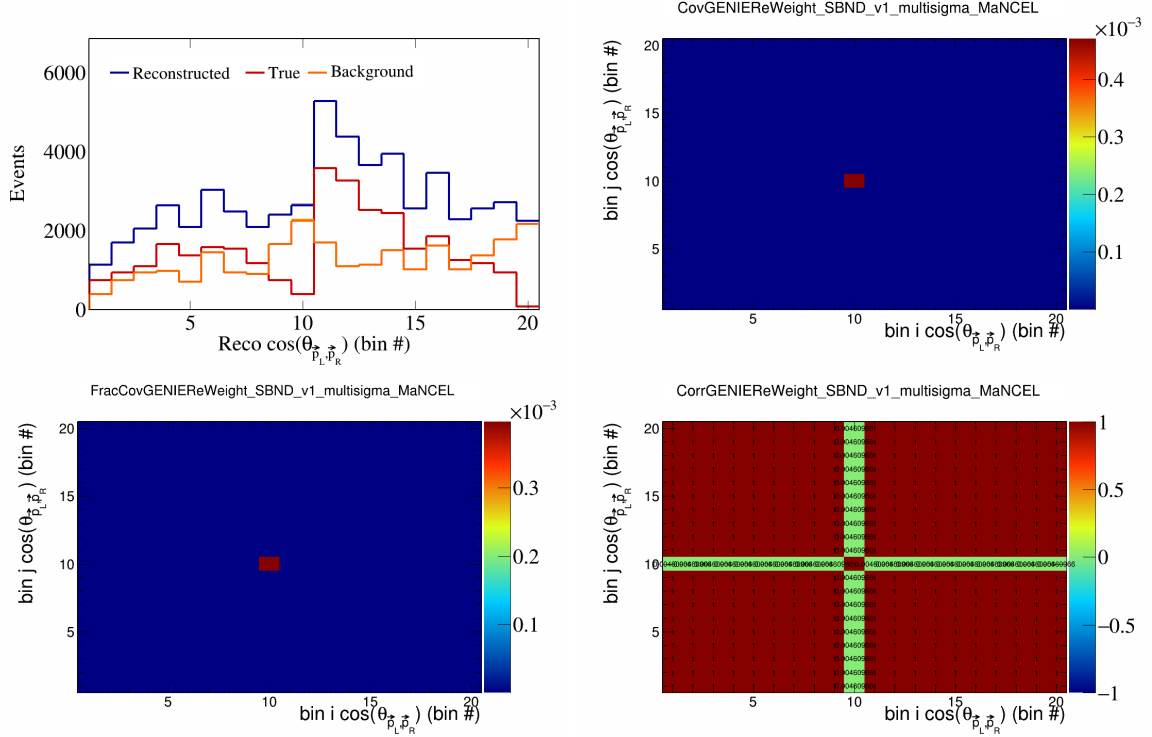


Figure 48: GenieMaNCEL variations for $\cos(\theta_{\vec{p}_L, \vec{p}_R})$ in $\cos(\theta_{\vec{p}_\mu})$.

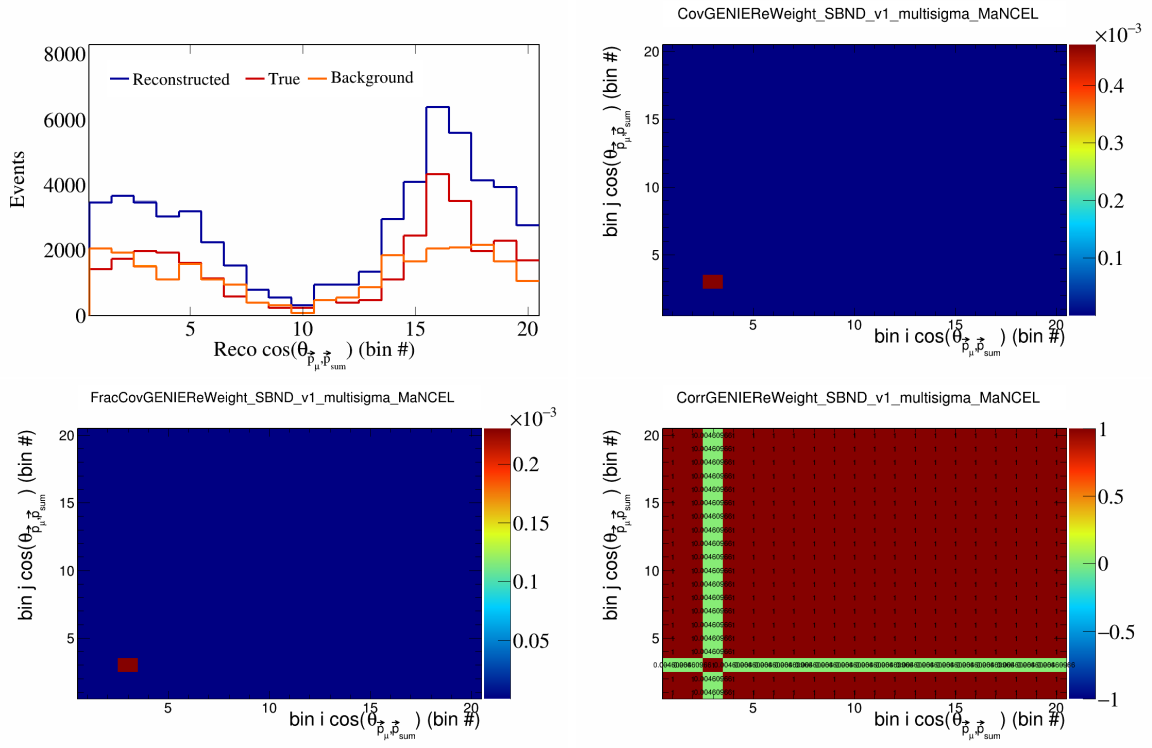


Figure 49: GenieMaNCEL variations for $\cos(\theta_{\vec{p}_\mu, \vec{p}_{\text{sum}}})$ in $\cos(\theta_{\vec{p}_\mu})$.

173 6 References

- 174 [1] C. Andreopoulos, A. Bell, D. Bhattacharya, F. Cavanna, J. Dobson, S. Dytman, H. Gallagher, P. Gu-
175 zowski, R. Hatcher, P. Kehayas, A. Meregaglia, D. Naples, G. Pearce, A. Rubbia, M. Whalley, and
176 T. Yang. The genie neutrino monte carlo generator. *Nuclear Instruments and Methods in Physics*
177 *Research Section A: Accelerators, Spectrometers, Detectors and Associated Equipment*, 614(1):87–104,
178 2010.
- 179 [2] Costas Andreopoulos, Christopher Barry, Steve Dytman, Hugh Gallagher, Tomasz Golan, Robert
180 Hatcher, Gabriel Perdue, and Julia Yarba. The genie neutrino monte carlo generator: Physics and
181 user manual, 2015.
- 182 [3] D. Ashery, I. Navon, G. Azuelos, H. K. Walter, H. J. Pfeiffer, and F. W. Schlepütz. True absorption
183 and scattering of pions on nuclei. *Phys. Rev. C*, 23:2173–2185, May 1981.
- 184 [4] P. S. Auchincloss, R. Blair, C. Haber, E. Oltman, W. C. Leung, M. Ruiz, S. R. Mishra, P. Z. Quintas,
185 F. J. Sculli, M. H. Shaevitz, W. H. Smith, F. S. Merritt, M. Oreglia, P. Reutens, R. Coleman, H. E. Fisk,
186 D. Levinthal, D. D. Yovanovitch, W. Marsh, P. A. Rapidis, H. B. White, A. Bodek, F. Borcherding,
187 N. Giokaris, K. Lang, and I. E. Stockdale. Measurement of the inclusive charged-current cross section
188 for neutrino and antineutrino scattering on isoscalar nucleons. *Zeitschrift für Physik C Particles and*
189 *Fields*, 48(3):411–431, Sep 1990.
- 190 [5] Ch. Berger and L. M. Sehgal. Lepton mass effects in single pion production by neutrinos. *Phys. Rev.*
191 *D*, 76:113004, Dec 2007.
- 192 [6] Ch. Berger and L. M. Sehgal. Partially conserved axial vector current and coherent pion production by
193 low energy neutrinos. *Phys. Rev. D*, 79:053003, Mar 2009.
- 194 [7] B. Bourguille, J. Nieves, and F. Sánchez. Inclusive and exclusive neutrino-nucleus cross sections and
195 the reconstruction of the interaction kinematics. *Journal of High Energy Physics*, 2021(4):4, Apr 2021.
- 196 [8] R.C. Carrasco and E. Oset. Interaction of real photons with nuclei from 100 to 500 mev. *Nuclear*
197 *Physics A*, 536(3):445–508, 1992.
- 198 [9] Jonathan Engel. Approximate treatment of lepton distortion in charged-current neutrino scattering
199 from nuclei. *Phys. Rev. C*, 57:2004–2009, Apr 1998.
- 200 [10] T. Golan, J.T. Sobczyk, and J. Źmuda. Nuwro: the wrocław monte carlo generator of neutrino interac-
201 tions. *Nuclear Physics B - Proceedings Supplements*, 229–232:499, 2012. Neutrino 2010.
- 202 [11] Krzysztof M. Graczyk and Jan T. Sobczyk. Form factors in the quark resonance model. *Phys. Rev. D*,
203 77:053001, Mar 2008.
- 204 [12] Yoshinari Hayato and Luke Pickering. The neut neutrino interaction simulation program library. *The*
205 *European Physical Journal Special Topics*, 230(24):4469–4481, Dec 2021.
- 206 [13] Konstantin S. Kuzmin, Vladimir V. Lyubushkin, and Vadim A. Naumov. Lepton polarization in neu-
207 trino–nucleon interactions. *Modern Physics Letters A*, 19(38):2815–2829, 2004.
- 208 [14] T. Leitner, L. Alvarez-Ruso, and U. Mosel. Charged current neutrino-nucleus interactions at interme-
209 diate energies. *Phys. Rev. C*, 73:065502, Jun 2006.
- 210 [15] C.H. Llewellyn Smith. Neutrino reactions at accelerator energies. *Physics Reports*, 3(5):261–379, 1972.
- 211 [16] Ulrich Mosel. Neutrino event generators: foundation, status and future. *Journal of Physics G: Nuclear*
212 *and Particle Physics*, 46(11):113001, sep 2019.
- 213 [17] J. Nieves, J. E. Amaro, and M. Valverde. Inclusive quasielastic charged-current neutrino-nucleus reac-
214 tions. *Phys. Rev. C*, 70:055503, Nov 2004.

- 215 [18] J. Nieves, F. Sánchez, I. Ruiz Simo, and M. J. Vicente Vacas. Neutrino energy reconstruction and the
216 shape of the charged current quasielastic-like total cross section. *Phys. Rev. D*, 85:113008, Jun 2012.
- 217 [19] J. Nieves, I. Ruiz Simo, and M. J. Vicente Vacas. Inclusive charged-current neutrino-nucleus reactions.
218 *Phys. Rev. C*, 83:045501, Apr 2011.
- 219 [20] J. Schwehr, D. Cherdack, and R. Gran. Genie implementation of ific valencia model for qe-like 2p2h
220 neutrino-nucleus cross section, 2017.
- 221 [21] Torbjörn Sjöstrand, Stephen Mrenna, and Peter Skands. Pythia 6.4 physics and manual. *Journal of
222 High Energy Physics*, 2006(05):026, may 2006.
- 223 [22] Júlia Tena-Vidal, Costas Andreopoulos, Adi Ashkenazi, Christopher Barry, Steve Dennis, Steve Dyt-
224 man, Hugh Gallagher, Steven Gardiner, Walter Giele, Robert Hatcher, Or Hen, Libo Jiang, Igor D.
225 Kakorin, Konstantin S. Kuzmin, Anselmo Meregaglia, Vadim A. Naumov, Afroditi Papadopoulou,
226 Gabriel Perdue, Marco Roda, Vladyslav Syrotenko, and Jeremy Wolcott. Neutrino-nucleon cross-section
227 model tuning in genie v3. *Phys. Rev. D*, 104:072009, Oct 2021.
- 228 [23] U. K. Yang and A. Bodek. Parton distributions, d/u , and higher twist effects at high x . *Phys. Rev.
229 Lett.*, 82:2467–2470, Mar 1999.